Supporting Online Material (SOM)

Mechanical control of tissue morphogenesis
by the Fat/Dachsous/Four-jointed planar cell polarity pathway

Floris Bosveld[1,*], Isabelle Bonnet[1,*], Boris Guirao[1,*], Sham Tlili[1,‡], Zhimin Wang[1], Ambre Petitalot[1], Raphaël Marchand[1], Pierre-Luc Bardet[1], Philippe Marcq[2], François Graner[1], Yohanns Bellaïche[1,♯]

[1] Polarity Division and Morphogenesis team, Institut Curie, CNRS UMR 3215, INSERM U934, 26 rue d'Ulm, 75248 Paris Cedex 05, France.
[2] Laboratoire Physico-Chimie Curie, Institut Curie, CNRS UMR 168, Université Pierre et Marie Curie, 26 rue d'Ulm, 75248 Paris Cedex 05, France.
∗ These authors contributed equally to this work
‡ Present address: Matière et Systèmes Complexes, Université Paris Diderot, CNRS UMR 7057, 10 rue Alice Domon et Léonie Duquet, 75205 Paris Cedex 13, France
♯ Corresponding author: yohanns.bellaiche@curie.fr

Contents

1 Materials and methods

1.1 Fly stocks and genetics

Fly stocks used in this study: *UAS-ds* (1), *tub-FRT-GAL80-FRT-GAL4 UAS-mRFP* (gift from E. Martin-Blanco), *UAS-fj*$^{[1062]}$ *UAS-fj*$^{[1762]}$ (2), *ubi-E-Cad:GFP* (3), *E-Cad:GFP* (4), *fj*$^{[P1]}$ (5), *dachs*$^{[GC13]}$ *FRT40A* (6), *dachs*$^{[210]}$ *FRT40A* (6), *fat*$^{[1]}$ *FRT40A* (6), *fat*$^{[8]}$ *dachs*$^{[GC13]}$ *FRT40A* (6), *fat*$^{[G-rv]}$ *FRT40A* (7), *sqh:mCherry* (8); fly stocks from the Bloomington Stock Center: *ds*$^{[05142]}$, *act5C-GAL4*$^{[25FO1]}$, *tub-GAL4*$^{[LL7]}$, *tub-GAL80ts*$^{[10]}$, *tub-GAL80ts*$^{[2]}$, *UAS-fat*$^{RNAi[TRiP.JF03245]}$, *UAS-ds*$^{RNAi[TRiP.JF02842]}$, *ubi-mRFP.nls FRT80B*; fly stock from the VDRC Stock Center: *UAS-dachs*$^{RNAi[v12555]}$. A *ubi-E-Cad:GFP* insertion on the third chromosome was made by mobilizing the *ubi-DE-Cad:GFP* present on the second chromosome (3).

In all experiments the white pupa stage was set to 0 hour after pupa formation (hAPF), determined with 1 h precision. Mutant clones in the scutellum were generated using FLP/FRT mediated mitotic recombination (9, 10). Clones were induced in second instar larvae by heat shock (20 min at 37°C). Clonal overexpression was achieved using a flip-out strategy (11) using the *tub-FRT-GAL80-FRT-GAL4* transgene. Overexpression studies were carried out using the *GAL4/UAS* system (12).

Temporal control of gene function was achieved by using the temperature sensitive *GAL80ts* (13). Embryos and larvae were raised at 18°C. Late third instar larvae were switched to 29°C. After 24 to 30 h, pupae were examined. Those which were timed as 11±1 hAPF were mounted for live imaging at 29°C. Some others were not mounted but kept further at 29°C until a total of 48 h, transferred back to 18°C, allowed to develop until adult stage, then photographed to quantify the shape of adult scutella.

1.2 Molecular biology

To create a D:GFP transgene under the control of its endogenous promoter, we used recombineering (14, 15) to introduce a GFP tag at the C-terminus of the *dachs* CDS present in BAC clone CH322-153C02 (BACPAC Resources Center). First a galK cassette, amplified with primers F (5'-CACAA GGGGCAGAGCTTCCACGTTCCCTTCCAGTTCATGACGCTCAGTAAACCTGTTGACAATTAATCA TCGGCA-3') and R (5'-CAGATGGAATGAATGGAATCATAACCAGTTTGTTTCCACCAGTAGTCCTT ATTCAGCACTGTCCTGCTCCTT-3') (underscored letters for galK sequences), was inserted *via* recombination at the C-terminus of the *dachs* CDS. After positive selection the galK cassette was replaced with the GFP tag, primers F (5'-CACAAGGGGCAGAGCTTCCACGTTCCCTTCCAGTTCATGACGCTCAGTA AAATGGTGAGCAAGGGCGAGGA-3') and R (5'-CAGATGGAATGAATGGAATCATAACCAGTTTGT TTCCACCAGTAGTCCTTACTTGTACAGCTCGTCCATGC-3') (underscored letters for GFP sequences) *via* recombination and negative selection for galK. The resulting attB-P[acman-d:GFP]-CmR-BW was integrated into the PBac{y[+]-attP-9A}VK00019 landing site at 68D2 creating *d:GFP*$^{[VK19]}$. As a control the untagged attB-P[acman-dachs]-CmR-BW was also integrated at this site, *dachs*$^{[VK19]}$. Both *d:GFP*$^{[VK19]}$ and *dachs*$^{[VK19]}$ rescue morphological defects and the viability of *dachs*$^{[GC13]}$/*dachs*$^{[210]}$ animals.

The ubi-Baz:mCherry transgene was constructed from pUASp-Baz-GFP (16). First the GFP was removed by

digestion with NotI/XbaI and replaced with mCherry, amplified with primers F (5'-GACGGCGGCCGCAAT GGTGAGCAAGGGCGAG-3') and R (5'-CCGTCTAGATTACTTGTACAGCTCGTCC-3'), and digested with NotI/XbaI, resulting in pUASp-Baz-mCherry. Next, a KpnI-XbaI fragment containing Baz:mCherry was isolated from pUASp-Baz:mCherry and inserted, using identical restriction sites, between the ubiquitin promoter and hsp27 terminator present in a modified pCasper4 (`http://flybase.org`). A ubi-H2B:RFP transgene was constructed by removing an Acc65I-XbaI fragment from pUAST-H2B:RFP (17) containing H2B:RFP and inserting it using identical restriction sites between the ubiquitin promoter and hsp27 terminator present in a modified pCasper4. All transgeneses were performed by Bestgene.

1.3 Immunohistochemistry and fixed tissue imaging

For fixed tissue analyses, pupae were dissected at 18-20 hAPF as previously described (18). Primary antibodies used were: rat anti-Fj (1:250) (19), rat anti-Ds (1:2000) (20), rabbit anti-Ds (1:500) (21), rabbit anti-β-galactosidase (1:2000) (Cappel Laboratories), rabbit anti-GFP (1:2000) (Molecular Probes), rat anti-Fat (1:1000) (20), rat anti-DE-Cad (1:100) (DSHB, DCAD2). Secondary antibodies used were: Alexa-488-conjugated goat-anti-rabbit IgG (Molecular Probes), Cy2-conjugated donkey-anti-mouse IgG (Jackson ImmunoResearch), Cy3-conjugated donkey-anti-mouse IgG (Jackson ImmunoResearch), Cy5-conjugated donkey-anti-rat IgG (Jackson ImmunoResearch). Images were collected with a confocal microscope (LSM 710 NLO, Carl Zeiss). All images represent maximum projections of a Z-stack unless otherwise specified.

LacZ enhancer trap lines were used to reveal the gene expression domains of *fj*, $fj^{[P1]}$ (5), and *ds*, $ds^{[05142]}$ (22). To quantify the opposing expression gradients of *fj* and *ds*, heterozygous $fj^{[P1]}$ (5) pupae (20 hAPF) were fixed and labeled with antibodies against β-galactosidase to reveal the *fj-lacZ* enhancer trap expression and antibodies against Ds to reveal the Ds protein gradient. Expression maps (1880×1770 pixels) were averaged over 7 different pupae aligned according to the positions of the macrochaetae which were determined by membrane staining with antibodies against E-Cadherin. Histograms of Fj and Ds images were equalized and normalized between 0 and 1. Subtracting Ds from Fj resulted in an image in arbitrary unit in the range $[-1; 1]$. A Gaussian lowpass filter of size 150 pixels with standard deviation 50 pixels was applied and the resulting image represented as a filled contour plot where the Λ shape appears as the orange band, of value ~ -0.2 (Fig. 2A).

From 29 hAPF onwards, the anterior-posterior boundary between the scutellum and the scutum can be easily distinguished since the scutellum and scutum are separated by rows of smaller cells. Therefore the position of the boundary can be precisely positioned on time-lapse movies by tracking back this group of smaller cells at earlier time-points. This reveals that the anterior-posterior boundary between the scutellum and the scutum has an indented shape from 11 hAPF onwards; and that it is positioned between the group of large and small cells located between the posterior dorso-central and the anterior scutellar macrochaetae. On fixed tissue at 20 hAPF, the anterior-posterior boundary between the scutellum and the scutum can be approximately positioned using these criteria.

1.4 S2 cell culture and immunoprecipitation

For cell culture experiments, a full length Dachs cDNA was Gateway cloned into pUbi-W-GFP (Drosophila Genomics Resource Center) creating ubi-D:GFP. The Ds intra cellular domain (aa 3115 to 3557) was inserted by Gateway cloning in pActin-Flag-W (Drosophila Genomics Resource Center) resulting in pActin-Flag:Ds^{intra}.

Drosophila S2 cells were maintained at 25°C in Schneider's Drosophila Medium (Gibco), containing 10% fœtal bovine serum inactivated at 65°C, penicillin (50 mg/ml) and streptomycin (50 mg/ml) (Gibco).

1.8×10^7 cells were transfected with expression vectors by the Effecten method (Qiagen), and 72 h post transfection, cells were lysed at 4°C in lyses buffer: 50 mM Tris-HCl (pH 8), 150 mM NaCl, 1 mM EDTA, 5 mM glycophosphate, 0.1% Triton and protease inhibitor cocktail (Sigma). Total protein levels were determined by the Bradford method (Bio-Rad). For immunoprecipitation, lysates were incubated with rabbit-anti-eGFP antibodies coupled to protein A agarose beads. Cell lysates and immunoprecipitates were separated by SDS-PAGE, transferred to PVDF membranes (Millipore) and probed with mouse anti-Flag primary antibodies (Sigma) and subsequently with HRP-conjugated anti-mouse secondary antibodies (Jackson ImmunoResearch). Western blots were revealed by an enhanced chemiluminescence (ECL) detection system according to the manufacturer's instructions (Amersham Biosciences).

1.5 Live imaging

1.5.1 Microscopy

Pupae were prepared for live imaging as described in (23). Typically pupae were imaged for a period of 15-26 h, starting at 11-12 hAPF, with an inverted confocal spinning disk microscope (Nikon) equipped with a CoolSNAP HQ2 camera (Photometrics) and temperature control chamber, using Metamorph 7.5.6.0 (Molecular Devices) with autofocus.

Single position movies in the scutellum were acquired at either 25±1°C or 29±1°C, with a 5 min temporal resolution (16-28 slices Z-stack, 0.5 μm/slice for ubi-E-Cad:GFP, E-Cad:GFP and 20-50 slices Z-stack, 0.3 μm/slice for D:GFP, ubi-Baz:mCherry). Acquiring 24 positions every 5 minutes (Z-stacks, 30 slices, 0.5 μm/slice) yielded a tiling of the whole dorsal thorax (311 frames).

1.5.2 Image treatment

Movies of ubi-E-Cad:GFP and E-Cad:GFP are maximum projections of Z-stacks, D:GFP and Sqh:mCherry are average projections. They were obtained using a custom ImageJ routine (publicly available as the "Smart Projector" plugin) and have been used for tissue flow analysis. Multiple position movies were stitched using a customized version of the "StackInserter" ImageJ plugin. Image dynamics is defined as the decimal logarithm of the ratio of the largest to smallest scale, expressed in "decades" or "orders of magnitudes". Here, with 5 min temporal resolution over 26 h of development and 0.32 μm spatial resolution over the 750×700 μm^2 of the tissue, we follow the $\sim 10^4$ cells with a dynamics of ~ 3 decades in both space and time.

Movies of D:GFP and ubi-Baz:mCherry are average projections of Z-stacks. They were obtained using a

custom Matlab routine that automatically detects the local Z level showing the higher apical Baz:mCherry signal and removes the underlying background signal, then projects slices around this Z level.

During the process of projection we kept records of slices containing the adherens junctions (*i.e.* the maximum intensity positions along the Z axis. We thus established topographical maps $Z(X, Y)$ across the plane. The angle with the horizontal plane, θ_{tilt}, is at most 0.01 radian over the scutellum, and reaches 0.02 radian only in the most lateral parts of the scutum. In the results presented here, the absolute correction due to this angle is thus negligible, $(1 - \cos\theta_{tilt}) \sim 10^{-4}$, and the curvature correction due to the spatial derivative of θ_{tilt} is negligible too.

1.6 Junction tension measurement by ablation

1.6.1 Laser ablation of individual cell junctions

Baz:mCherry and D:GFP scutellum tissues were imaged using a two-photon laser-scanning microscope (LSM 710 NLO, Carl Zeiss) in single-photon mode at a resolution of 100×100 pixels (pixel size = 0.18 μm) with a bidirectional scan lasting $\delta t = 156$ ms. We used the 488 nm laser for D:GFP and the 561 nm one for Baz:mCherry. "Low" and "high" D:GFP cell junctions were individually ablated using a Ti:Sapphire laser (Mai Tai DeepSee, Spectra Physics) at 890 nm with < 100 fs pulses with a 80 MHz repetition rate. The laser power (typically ~ 0.2 W at the back focal plane) was chosen to ablate a cell junction without creating cavitation (24).

Ablations at junctions between wt and $fat^{[G-rv]}$ cells, and control ablations between differently marked wt cells, were performed in pupae expressing both Baz:mCherry and D:GFP. Ablations of junctions between wt and $fat^{[8]}$ $dachs^{[GC13]}$ cells were performed in pupae expressing only Baz:mCherry. All ablations were performed in the scutum to avoid the endogenous polarization of Dachs.

1.6.2 Quantification of junction tension

Junction tension prior to ablation and relaxation speed of ablated junction vertices immediately after ablation are considered to be proportional (25–28). Baz:mCherry images were first denoised using Safir software (29) to improve the vertex localization accuracy. To determine the initial relaxation speed, the vertex-vertex distance d_{vv} of the pre-cut and post-cut ablated junction was measured manually (in blind procedure) using ImageJ at $n = 2$ and $n = 10$ frames after ablation.

Since the relaxation deviates from linearity already in the first 10 time steps, the measured relaxation speeds $V_2 = \frac{d_{\mathrm{vv}}(2\delta t) - d_{\mathrm{vv}}(0)}{2\delta t}$ and $V_{10} = \frac{d_{\mathrm{vv}}(10\delta t) - d_{\mathrm{vv}}(0)}{10\delta t}$ are not equal. However, they are roughly proportional to each other, so that the conclusions obtained in Fig. 3E are robust with respect to the choice of n. Their *amplitude* does not correlate with the direction of the ablated junction prior to ablation (fig. S8). Conversely, as expected, the *direction* of the tension, and thus of the relaxation speed, fully correlates with the direction of the junction prior to ablation.

Statistical tests for data significance were performed using the Matlab's built-in function `ttest2.m` (two-sample t-test).

2 Quantitative data analysis

In our mechanical description, the local velocity describes the movements in the scutum and the scutellum. It includes all contributions to tissue morphogenesis regardless of their cellular origin, such as cell shape changes, rearrangements, divisions, apoptoses.

As described in fig. S19 or in ref. (30), a translation and a rotation (represented as an arrow and a circle, respectively) are movements which preserve the relative positions of cells. Change of size and/or shape thus results from velocity of tissue parts relative to each other: this is measured by the space variation of the velocity, *i.e.* velocity gradient, also called "deformation rate", and represented as an ellipse. Removing the size change from the deformation rate characterizes specifically the morphogenesis, *i.e.* change of shape: this is measured by the "contraction rate", and represented as a blue bar. We now develop these points one by one; for more details, refer to textbooks (31, 32).

2.1 Quantification of tissue flow fields

2.1.1 Velocimetry

The local tissue flow within scutum and scutellum tissues was quantified using movies of pupae expressing E-Cad:GFP or Baz:mCherry. For each movie, the flow field was obtained by image cross-correlation (IC) velocimetry along sequential images using customized Matlab routines based on the particle image velocimetry (33) toolbox, matpiv (`http://folk.uio.no/jks/matpiv`). Each image correlation window (hereafter "IC-box") was a 64×64 pixels square ($\sim$ 20×20 μm^2, pixel size 0.32 μm), had a 50% overlap with each of its neighbors, and typically contained a few tens of cells: this size corresponded to an optimum in the signal-to-noise ratio.

In each IC-box (i, j), the velocity field $\mathbf{V}(i, j, t)$ was measured by correlating two successive images, at times t and $t + \Delta t$ separated by $\Delta t = 5$ min, and by performing a sliding average over $24\Delta t = 2$ h to improve the signal to noise ratio without loss of information. The velocity field $\mathbf{V}$ was represented with *arrows*, expressed in μm.min^{-1}. The tissue flow was identical when measured with E-Cad:GFP or Baz:mCherry. Within any single pupa where both hemi-scutella were imaged, the flow field appeared precisely symmetrical with respect to the midline: this acted as a control of the reliability of velocity measurements.

2.1.2 Tissue flow representations

Differentiating the velocity field yields the velocity gradient matrix, $\overline{\overline{\nabla \mathbf{V}}}$:

$$\overline{\overline{\nabla \mathbf{V}}} = \begin{pmatrix} \frac{\partial V_x}{\partial x} & \frac{\partial V_y}{\partial x} \\ \frac{\partial V_x}{\partial y} & \frac{\partial V_y}{\partial y} \end{pmatrix} . \tag{1}$$

It is expressed in min^{-1}; note that 10^{-3} min^{-1} = 1/(1000 min) corresponds to a relative change of 1% in 10 min.

To represent it, three quantities derived from it, also expressed in min^{-1}, were computed and represented, as explained in fig. S19: the local deformation rate, contraction-elongation rate, and rotation rate. Mathematically, these quantities are defined as follows:

• The *deformation rate*, $\overline{\overline{\nabla \mathbf{V}}}^{sym}$. It is the symmetrized part of the velocity gradient:

$$\overline{\overline{\nabla \mathbf{V}}}^{sym} = \begin{pmatrix} \frac{\partial V_x}{\partial x} & \frac{1}{2}\left(\frac{\partial V_x}{\partial y} + \frac{\partial V_y}{\partial x}\right) \\ \frac{1}{2}\left(\frac{\partial V_x}{\partial y} + \frac{\partial V_y}{\partial x}\right) & \frac{\partial V_y}{\partial y} \end{pmatrix} = \begin{pmatrix} \nabla V_{xx}^{sym} & \nabla V_{yx}^{sym} \\ \nabla V_{xy}^{sym} & \nabla V_{yy}^{sym} \end{pmatrix} . \tag{2}$$

Since $\overline{\overline{\nabla \mathbf{V}}}^{sym}$ is a 2D symmetric matrix, it can be diagonalized and represented as an *ellipse* (fig. S19). which axis lengths are proportional to the two eigenvalues. A positive eigenvalue corresponds to a direction of elongation represented in red. Conversely, a negative eigenvalue corresponds to a direction of contraction represented in blue. Four possible cases are thus represented by four types of ellipses. (i) A positive isotropic dilation corresponds to two equal red bars. (ii) An ellipse with a red bar and a smaller blue bar is a traceless contraction-elongation plus a positive isotropic dilation. (iii) An ellipse with a red bar and a larger blue bar is a traceless contraction-elongation plus a negative isotropic dilation. (iv) A negative isotropic dilation corresponds to two equal blue bars.

• The *contraction-elongation rate*, $\overline{\overline{\nabla \mathbf{V}}}^{dev}$. It is obtained from the decomposition of $\overline{\overline{\nabla \mathbf{V}}}^{sym}$ into two contributions: its trace $\mathrm{Tr}\left(\overline{\overline{\nabla \mathbf{V}}}^{sym}\right)$, which reflects the overall isotropic dilation rate of apical area; and the traceless remaining part, also called the "deviator", $\overline{\overline{\nabla \mathbf{V}}}^{dev}$:

$$\overline{\overline{\nabla \mathbf{V}}}^{sym} = \frac{1}{2}\mathrm{Tr}\left(\overline{\overline{\nabla \mathbf{V}}}^{sym}\right)\bar{\bar{\mathbf{I}}} + \overline{\overline{\nabla \mathbf{V}}}^{dev} , \tag{3}$$

where $\bar{\bar{\mathbf{I}}} = \begin{pmatrix} 1 & 0 \\ 0 & 1 \end{pmatrix}$ is the identity matrix. Since $\overline{\overline{\nabla \mathbf{V}}}^{dev}$ is symmetric and traceless, it can be diagonalized with its two opposed eigenvalues $\pm\lambda$, which represent the rate of contraction in one direction and an equal rate of elongation in the perpendicular direction (and thus an effective change in tissue shape), at fixed apical area. Such traceless contraction-elongation corresponds to two orthogonal bars of equal lengths, one blue, one red. Since they are redundant, for clarity in all figures we plot only one: we choose the *blue bar* of length $|\lambda|$ in the direction of contraction (fig. S19).

• The *rotation rate*, ω. It is the anti-symmetric part of $\overline{\overline{\nabla \mathbf{V}}}$:

$$\omega = \frac{1}{2}\left(\frac{\partial V_y}{\partial x} - \frac{\partial V_x}{\partial y}\right) . \tag{4}$$

This is a real number; it is represented as a *circle*, which diameter is the rotation rate $|\omega|$, and which color reflects its sign: red is for clockwise rotation and blue is for counter-clockwise (fig. S19).

2.2 Comparing and averaging different movies

We aimed at averaging different hemi-scutellum movies corresponding to the same genotype, or comparing movies corresponding to different genotypes. For that purpose, their common space and time coordinates were defined as follows.

2.2.1 Space registration

Each hemi-scutellum movie was oriented with the midline along the top horizontal side. Spatial landmarks (fig. S4A) were the positions of the two scutellar macrochaetae at 16:30 hAPF, when the sensory organ

precursor (SOP) cells divide (34), and the results were independent of the choice of this reference time. The posterior scutellar macrochaeta defines the X axis and the lateral scutellar macrochaeta sets the Y axis. We find that the positions of macrochaetae are reproducible up to 15 μm. The intersection of these X and Y axes defines the origin of the IC-grid, whereby (0,0) is centered around one IC-box (green dashed square in fig. S4A). Each IC-box is then labelled by two integer numbers (i, j) which define our two-dimensional space coordinates on a fixed square lattice (Eulerian representation). Averaging over space is implemented by averaging over (i, j).

2.2.2 Time registration

While the hAPF was determined with 1 h absolute precision, the tissue rotation rate analysis provided a better relative precision that we used to synchronize the different movies, as follows. In the region of the tissue located near the origin of axes, we observed that the rotation rate (Eq. 4) systematically passed through a maximum during the development: this rotation peak could be used as a biological reference time. For that purpose, the rotation rate was measured and spatially integrated over a rectangular reference window (IC-boxes labelled $i = -2$ to 6 and $j = -2$ to 2). Plotting this average, $\bar{\omega}_{\text{ref window}}$, versus frame number yielded a bell-shaped curve (fig. S4B).

We applied a time translation to each movie so that these curves overlapped. We matched the portion of the curve which had the steepest slope (fig. S4B'): we thus used the time corresponding to 3/4 of the peak value, in the ascent (rather than the maximum itself, which by definition had a vanishing slope). Its value, averaged over $n = 11$ wt tissue movies was 18:40 hAPF. Hereafter, "hAPF" indicates the time after this temporal translation has been applied. For instance, after synchronization, the maximum of the contraction-elongation and rotation rates were consistently found at 19:20 and 19:40 hAPF, respectively. This determination reached a $\pm$ 1 interframe (*i.e.* $\pm$5 min) relative precision in wt.

For experiments performed at 29°C, the development is accelerated. This was taken into account by dividing time intervals by 0.9 (as determined with $\pm$0.05 precision by the widening of the wt rotation peak). Mutant tissues were synchronized with the same procedure as the wt tissue, up to a 10 min precision (fig. S20).

2.2.3 Ensemble average

These spatial and temporal adjustments allowed us to assign a system of space-time coordinates (i, j, t) common to any set of N hemi-scutellum movies, from pupae with a given genotype g (wt or mutant). We defined the ensemble averaged deformation rate:

$$\overline{\overline{\nabla \mathbf{V}}}_g^{sym}(i,j,t) = \frac{1}{N}\sum_{n=1}^{N} \overline{\overline{\nabla \mathbf{V}}}_g^{sym}(i,j,t,n)\ . \tag{5}$$

as well as its standard deviation $\delta_g\left[\overline{\overline{\nabla \mathbf{V}}}^{sym}\right]$. Averages and standard deviations were measured over the space-time points (i, j, t) for which experimental data were available in all movies after synchronization (intersection of the data). Since $\delta_g\left[\overline{\overline{\nabla \mathbf{V}}}^{sym}\right]$ reflects our detection level, $\overline{\overline{\nabla \mathbf{V}}}_g^{sym}(i,j,t)$ was considered as significant if $|\lambda|(i,j,t)$ was larger than $\delta_g\left[\overline{\overline{\nabla \mathbf{V}}}^{sym}\right](t)$ and plotted as blue bars, else as gray bars (Fig. 4C,D and figs. S11A-C, S15A,B, S16C,D).

2.3 Quantification of D:GFP signal

Anisotropy of Dachs is due to a combination of cell shape anisotropy and of Dachs distribution around each given cell (section 2.3.4), which both contribute to stress (section 3.2.2). To quantify and average the Dachs signal distribution in wt hemi-scutella, we used movies of flies expressing both Baz:mCherry to label cell adherens junctions, and D:GFP. The tissue flow analysis was performed on Baz:mCherry in order to determine for all movies the spatio-temporal coordinates (i, j, t): these coordinates were then used for D:GFP signal quantification.

2.3.1 Anisotropy of D:GFP

The 2D Fourier transform (FT) is a classical tool to extract the orientations of geometric patterns in an image (35). For example, the FT of an image of a regular pattern (such as a sinusoidal grid, see fig. S10A) leads to a FT whose signal is mainly in the direction orthogonal to the grid (fig. S10B-C) and can be represented as a green bar (fig. S10D). More generally, an image can be decomposed into a set of frequencies which reflect the existence, the spacing and direction of geometric patterns.

To assess the anisotropy of D:GFP signal distribution in each IC-box (fig. S10E), its 2D discrete FT was performed using Matlab's built-in function `fft2.m`. In order to reduce spectral artifacts introduced by IC-box edges (35), the raw image was multiplied by a square cosine before computing its FT. To make the analysis robust with respect to possible translations of the D:GFP pattern within the IC-box, only the FT norm (and not its phase) was kept, and the same sliding average over 2 h as in flow analysis was performed to improve the signal to noise ratio. We determined its ensemble average over several movies, $\mathcal{F}(i, j, t)$ as well as the corresponding standard deviation $\delta[\mathcal{F}](t)$.

For each given (i, j, t), the FT's norm was a function of the Fourier reciprocal space coordinates, $\mathcal{F}(\tilde{x}, \tilde{y}, t)$, corresponding to a distribution of gray levels. It was maximal at the center, $(\tilde{x}, \tilde{y}) = (0, 0)$ and decreased faster in the direction of the D:GFP pattern anisotropy than in the orthogonal direction (fig. S10F). This function was binarized by keeping only the pixels $(\tilde{x}, \tilde{y})$ having gray levels above the 80^{th} percentile. Such thresholding yielded a cluster of points displaying anisotropically distributed positions $(\tilde{x}, \tilde{y})$ (fig. S10G). Its variance matrix $\begin{pmatrix} \overline{\tilde{x}^2} & \overline{\tilde{y}\tilde{x}} \\ \overline{\tilde{x}\tilde{y}} & \overline{\tilde{y}^2} \end{pmatrix}$ was then computed. The traceless part of this matrix had two opposed eigenvalues $\pm\mu$: here $|\mu|$ quantified the variance of D:GFP pattern anisotropy, so that $\sqrt{|\mu|}$ quantified its standard deviation. The eigenvector with a negative eigenvalue typically reflected the direction of the D:GFP pattern anisotropy.

2.3.2 Amount of D:GFP

In a semi-quantitative approach we constructed a number to quantify the observation that more contrasted parts of the image were the ones where D:GFP amount was larger. The local contrast $C(i, j, t)$ was thus defined as a relative intensity, as follows. We noted P_5 and P_{95} the average intensity of the pixels below the 5^{th} percentile and above the 95^{th} percentile, respectively. For each IC-box at a given space-time point

(i,j,t), we then constructed the number $C(i,j,t)$:

$$C(i,j,t) = \frac{P_{95}(i,j,t) - P_5(i,j,t)}{P_{95}(i,j,t)} \ . \tag{6}$$

$C(i,j,t)$ was found to range from 0.5 for lowest D:GFP signal regions up to 2 for highest D:GFP signal regions.

2.3.3 Representation of D:GFP polarization: $\overline{\overline{\mathbf{Q}}}$ matrix

To combine the quantifications of anisotropy and amount of D:GFP signal, a matrix $\overline{\overline{\mathbf{Q}}}(i,j,t)$ was built as follows. Its eigenvectors were those defined in section 2.3.1: they were typically parallel and orthogonal to the main anisotropy direction of the local D:GFP pattern. Its eigenvalues were defined as $\pm C(i,j,t)\sqrt{|\mu|(i,j,t)}$, where $\sqrt{|\mu|}$ quantified the standard deviation of the D:GFP pattern anisotropy, and the weight C quantified the amount of D:GFP (section 2.3.2). We ensemble averaged $\overline{\overline{\mathbf{Q}}}$ over $n = 3$ movies.

A *green bar* of length $C(i,j,t)\sqrt{|\mu|(i,j,t)}$ was plotted in the direction of the negative eigenvalue of $\overline{\overline{\mathbf{Q}}}$ (fig. S10H). The bar length and direction reflected the visible characteristics of the D:GFP pattern, which could be averaged. More precisely, we considered $\overline{\overline{\mathbf{Q}}}(i,j,t)$ as significant if $\sqrt{|\mu|(i,j,t)}$ was larger than $\delta\left[\mathcal{F}\right](t)$.

2.3.4 Comparisons of D:GFP, Sqh:mCherry and E-Cad:GFP anisotropies

As already mentioned, anisotropy of Dachs is due to a combination of cell shape anisotropy and of Dachs distribution around each given cell. To disentangle these effects, we measured the anisotropy $\sqrt{|\mu|(i,j,t)}$ of D:GFP, Sqh:mCherry and of E-Cad:GFP in $n = 3$ movies at 25°C for each condition (fig. S9G,G',H). The procedure was the same as in section 2.3.1, with the 70^{th} percentile instead of the 80^{th}, to adapt to the movies quality.

The Sqh:mCherry and E-Cad:GFP patterns are similar and reflect cell elongations (compare figs. S9G' and H). Almost everywhere, they are not significantly different from zero. They are just below or just above the threshold only at the few places where cells are much more elongated.

3 Theoretical model

We sought to investigate whether there was a connection between: (i) the observed D:GFP polarization; (ii) the Dachs-related contribution to mechanical stress; and (iii) the Dachs-related contribution to tissue flow. For that purpose, we have developed a physical model of the relation between stress and flow. This analysis led to the identification of relevant quantities: first, a matrix characterizing the contraction rate; second, a semi-quantitative estimate of stress based on a matrix characterizing Dachs polarization. Furthermore, the model predicted that these matrices were linked and were locally proportional to each other: this predictions was experimentally tested.

In short, the prediction of our physical model is: if D:GFP imposed a stress pattern to the tissue then for every mutant affecting Dachs polarization, we should observe that the difference in tissue contraction between this mutant and the wt condition should correlate with the D:GFP polarization pattern. Combining

physical modeling and subtractive approach thus extracts and evidences the contribution of a given individual pathway within an elaborated morphogenetic movement. It thus links genetics and mechanics in the context of tissue morphogenesis. We explicit the model in the context of the $dachs^{RNAi}$ mutant condition. Similar conclusions can be reached using the ds^{RNAi}, fat^{RNAi} or fj^{UP} mutant conditions which affect the pattern of Dachs polarization.

3.1 Hypotheses

We treated the flow in two dimensions because: (i) the dorsal thorax epithelium is a quasi-2D monolayered tissue with negligible curvature; (ii) the network of the adherens junction belts which we image, and which enables long-range transmission of in-plane stresses within tissues (36), is only a few μm thick; and (iii) the visible in-plane components of the tissue flow velocity likely dominate its possible out-of-plane components.

Developing tissues have been observed to display simultaneously liquid-like behaviours (flow at large scale), and solid behaviours (elastic deformations of cells, irreversible plastic shape changes) (37–39). However, under the effect of active cell shape fluctuations (37) the liquid behaviour dominates (37, 39, 40) at times larger than the characteristic visco-elastic time, which is reported to be of order of minutes (37, 39, 41). Here, morphogenetic movements had a time scale of the order of 2 hours (velocity gradients at most of a few hundredths of min^{-1}). We then safely assumed that the dominant contribution to mechanical stress $\overline{\overline{\sigma}}$ was viscous (37, 42) and wrote (43):

$$\overline{\overline{\sigma}} = \left[-p + 2\eta_{\mathrm{comp}}\ \mathrm{Tr}\left(\overline{\overline{\nabla \mathbf{V}}}^{sym}\right)\right]\overline{\overline{\mathbf{I}}} \ +\ 2\eta_{\mathrm{eff}}\ \overline{\overline{\nabla \mathbf{V}}}^{dev} \ . \tag{7}$$

Here p is the pressure; η_{comp} a compressibility dissipation, which includes several contributions; η_{eff} is the usual hydrodynamic viscosity: the subscript "eff" recalls that it is an effective viscosity which not only includes the contribution of cytoplasmic viscosity, but also active contributions from the cytoskeleton, or from neighbor rearrangements (37). The deformation rate $\overline{\overline{\nabla \mathbf{V}}}^{sym}$ and the contraction-elongation rate $\overline{\overline{\nabla \mathbf{V}}}^{dev}$ are defined in Eqs. (2,3); the traceless part of the stress $\overline{\overline{\sigma}}^{dev}$ is defined as in Eq. 3:

$$\overline{\overline{\sigma}}^{dev} = \overline{\overline{\sigma}} - \frac{1}{2}\ \mathrm{Tr}\left(\overline{\overline{\sigma}}\right)\overline{\overline{\mathbf{I}}} = 2\eta_{\mathrm{eff}}\ \overline{\overline{\nabla \mathbf{V}}}^{dev} \ . \tag{8}$$

Eq. 8, which is independent from the trace, reflects the contraction-elongation part of the flow, involved in changes of shape (*i.e.* morphogenetic movements), and of interest in what follows.

3.2 Subtractive method

3.2.1 Modeling

Since Eq. 8 is linear, one can use it to write the stress in presence of Dachs, that is, in the wt context, $\overline{\overline{\sigma}}^{dev}_{\mathrm{wt}}$, minus the stress in absence of Dachs, $\overline{\overline{\sigma}}^{dev}_{dachs^{RNAi}}$:

$$\overline{\overline{\sigma}}^{dev}_{\mathrm{wt}} - \overline{\overline{\sigma}}^{dev}_{dachs^{RNAi}} = 2\eta_{\mathrm{eff}}\left(\overline{\overline{\nabla \mathbf{V}}}^{dev}_{\mathrm{wt}} - \overline{\overline{\nabla \mathbf{V}}}^{dev}_{dachs^{RNAi}}\right) \ . \tag{9}$$

The left and right hand sides of Eq. 9 reflect the specific contribution of Dachs to the stress and to the flow, respectively. We introduce the compact notations:

$$\overline{\overline{\sigma}}_{\mathrm{Dachs}} \ = \ \overline{\overline{\sigma}}^{dev}_{\mathrm{wt}} - \overline{\overline{\sigma}}^{dev}_{dachs^{RNAi}} \ , \tag{10}$$

$$\overline{\overline{\nabla \mathbf{V}}}_{\mathrm{Dachs}} \ = \ \overline{\overline{\nabla \mathbf{V}}}^{dev}_{\mathrm{wt}} - \overline{\overline{\nabla \mathbf{V}}}^{dev}_{dachs^{RNAi}} \ . \tag{11}$$

In order to avoid confusion between the left and right hand sides of Eqs. 10,11, and since we only consider the traceless parts of matrices in what follows, we have dropped the *dev* superscript. Using these notations, Eq. 9 reads:

$$\overline{\overline{\sigma}}_{\mathrm{Dachs}} = 2\eta_{\mathrm{eff}}\overline{\overline{\nabla \mathbf{V}}}_{\mathrm{Dachs}} \, . \tag{12}$$

3.2.2 Measurable quantities

Eq. 12 establishes a proportionality relation between two quantities which can be measured in experiments. In the right hand side, $\overline{\overline{\nabla \mathbf{V}}}_{\mathrm{Dachs}}$ can be directly measured. In the left hand side, since Dachs-rich cell junctions were under a larger tension and were apparently distributed anisotropically, one could expect that Dachs had an anisotropic contribution to $\overline{\overline{\sigma}}_{\mathrm{Dachs}}$: it was stronger in the direction of strong Dachs intensity than in the perpendicular direction. This contribution to stress could be estimated by measuring both the length and tension of each cell-cell junction (44). Here the tension measurement required the quantitative determination of: (i) D:GFP amount based on fluorescent intensity, and (ii) of the relation between D:GFP quantity and tension. Both (i) and (ii) were beyond the scope of this study.

Instead, we used the matrix $\overline{\overline{\mathbf{Q}}}$ built in section 2.3.3 as a semi-quantitative measurement of Dachs distribution, combining both cell shape anisotropy and Dachs distribution around each given cell. In the case where Dachs was absent or isotropically distributed, the FT signal was zero or isotropic, and $\overline{\overline{\mathbf{Q}}}$ was zero by construction. Thus $\overline{\overline{\sigma}}_{\mathrm{Dachs}}$ and $\overline{\overline{\mathbf{Q}}}$ vanished simultaneously; in a linear approximation one could thus reasonably expect that they were proportional to each other:

$$\overline{\overline{\mathbf{Q}}} = \mathrm{cst} \times \overline{\overline{\sigma}}_{\mathrm{Dachs}} \, . \tag{13}$$

3.3 Predictions and experimental tests

3.3.1 Predictions regarding experiments

Combining Eqs. 12-13 immediately yields a testable relation between two operationally measurable quantities:

$$\overline{\overline{\mathbf{Q}}} = \mathrm{cst} \times \overline{\overline{\nabla \mathbf{V}}}_{\mathrm{Dachs}} \, . \tag{14}$$

Eq. 14 is our main prediction. It states that the distribution of Dachs planar polarization, measured by D:GFP FT, correlates with the local subtraction of $dachs^{RNAi}$ from wt contraction-elongation rates.

Eq. 14 can thus be tested by comparing the patterns of $\overline{\overline{\mathbf{Q}}}$ and $\overline{\overline{\nabla \mathbf{V}}}_{\mathrm{Dachs}}$ in the scutellum. If there was a direct or indirect causal relation between $\overline{\overline{\mathbf{Q}}}$ and $\overline{\overline{\nabla \mathbf{V}}}_{\mathrm{Dachs}}$, and if this relation was indeed local, then patterns of both matrix fields should look similar.

3.3.2 Tests

As a first test, one could perform a direct visual comparison of data. Indeed, after averaging over the time interval 17:20 - 21:20 hAPF where contraction-elongation was the largest, similar qualitative features were observed in the zones where $\overline{\overline{\mathbf{Q}}}$ or $\overline{\overline{\nabla \mathbf{V}}}_{\mathrm{Dachs}}$ were significant. The position, size and shape of these zones were similar in both patterns. Within these zones, the orientation of $\overline{\overline{\mathbf{Q}}}$ and $\overline{\overline{\nabla \mathbf{V}}}_{\mathrm{Dachs}}$ appeared similar (compare Figs. 4B and C; see also Fig. 4D).

To make this test more quantitative, we quantified the local alignment between the blue bars of the contraction rate and the green bars of D:GFP patterns. These bars made a relative angle noted $\alpha(i,j)$. Since bars were not oriented, α was defined modulo π, and the local alignment could be characterized by:

$$A(i,j) = \cos^2\alpha(i,j) \ . \tag{15}$$

The alignment coefficient $A(i,j)$ of $\overline{\overline{\nabla\mathbf{V}}}_{\mathrm{Dachs}}$ (or of any other matrix) with the FT pattern $\overline{\overline{\mathbf{Q}}}$ was coded in orange, from 0 for fully anti-correlated, to 1 for fully correlated, through 0.5 for non correlated (Fig. 4C'D', fig. S14C'D', fig. S16C'D'), on IC-boxes where both $\overline{\overline{\nabla\mathbf{V}}}_{\mathrm{Dachs}}$ and $\overline{\overline{\mathbf{Q}}}$ were significant. Averaging Eq. 15 over these IC-boxes yielded its spatial average, A (indicated on top right of panels such as Fig. 4C'):

$$A = \frac{\sum\limits_{i,j} w(i,j)\,\cos^2\alpha(i,j)}{\sum\limits_{i,j} w(i,j)} \ . \tag{16}$$

Here the weights $w(i,j)$ include the norms of both matrix fields, $w(i,j) = |\overline{\overline{\nabla\mathbf{V}}}_{\mathrm{Dachs}}(i,j)| \times |\overline{\overline{\mathbf{Q}}}(i,j)|$, averaged over 17:20 - 21:20 hAPF. In practice these weights have only a small effect on A values. A reflects the overall alignment of $\overline{\overline{\mathbf{Q}}}$ and $\overline{\overline{\nabla\mathbf{V}}}_{\mathrm{Dachs}}$. If the bars of $\overline{\overline{\nabla\mathbf{V}}}_{\mathrm{Dachs}}$ and $\overline{\overline{\mathbf{Q}}}$ remained always perfectly orthogonal or colinear, then $A = 0$ or 1, respectively. In between, A varied between 0 and 1. In the case where $\overline{\overline{\nabla\mathbf{V}}}_{\mathrm{Dachs}}$ and $\overline{\overline{\mathbf{Q}}}$ were not correlated, their relative angle α varied randomly, and $A \approx 0.5$. By running simulations with random angles, with same sample size as in our experiments, we estimated the standard deviation around the mean value $\langle A \rangle = 0.5$ to be $\sigma = 1.7 \times 10^{-2}$. We used this value to determine the significance of the difference ΔA between two measured values of A by calculating the p-value, $p = 1 - \mathrm{erf}(\Delta A/\sigma\sqrt{2})$ (45).

4 Segmented image analysis

To reinforce the multiscale description of morphogenetic movements, from cell level to tissue level, we performed detailed cell-level analysis. Images were denoised with the Safir software (29). Cell contours were determined and individual cells were identified using a standard watershed algorithm, followed by several rounds of manual corrections. Around 2.8 million cells (8.4 million cell-cell junctions) were segmented. Both by manual tests on small subsamples, and by automatic tracking of false cell appearances or disappearances, we estimated the error rate to be below 10^{-4}, which was sufficient for the analyses presented here.

4.1 Patterns of proliferation, cell apical area, and cell apical anisotropy

Four wt scutellum movies at 25°C were segmented over 156 frames. An in-house automatic software (Matlab) tracked segmented cells through all images. It yielded maps of cell centroid displacements (fig. S12C), cell lineages and lists of divisions (fig. S12B,C and Movie S2C,C'), and lists of apoptoses (Movie S2C,C').

We detected 1591 divisions with an error rate estimated below 1%. The wt movies were synchronized using IC analysis (section 2.2.2) to obtain an ensemble averaged number of divisions plotted versus hAPF with again a sliding average over 24 $\Delta t = 2$ h. A division angle Θ was defined as the angle between AP axis and the line connecting the centroids of the daughter cells in their first image of appearance. Division angles were scored for Θ in $[0°, 180°]$. For clarity, scores were represented in polar histograms ("rose plots") around the full circle by displaying both Θ and $\Theta + 180°$ (respectively dark blue and blue in fig. S12B).

For whole thorax movies (Movie S1), each image contained in average around 10^4 cells and parts of the movies were segmented. Measurements performed on single images yielded maps of cell apical area and anisotropy (Fig. 1C-D and fig. S1C,D). The cell division pattern reported in Fig. 1B was determined manually by visual tracking of cell divisions through all images. Cells in the anteriormost part get out of focus due to tissue flow and elongation, so that we cannot determine the total number of cell divisions that they undergo (gray cells in Fig. 1B).

4.2 Cell shape changes and rearrangements

To quantify cell shape changes, Rauzi *et al.* (see the figs. 5a and S4 of ref. (26)) used a matrix called "texture" as defined in Eq. 6 of ref. (46). It is based on the links connecting each cell center with the centers of its neighbors: it expresses, in μm^2, the variance of link length in each direction. Separately, rearrangements were counted and quantified as integer numbers. Similarly, Aigouy *et al.* (47) used a former version of the texture as defined in the Eq. 1 of ref. (48), which expressed the variance of the cell junctions in each direction. More precisely, they call "cell elongation" (defined in Eq. S25 of ref. (47)) the traceless part of the texture. Again, rearrangements were quantified separately, and as integer numbers (see Fig. 4 of ref. (47)). Note that in a rearrangement a cell junction vanishes and a new junction is created. It is sometimes followed by the opposite rearrangement, where the new junction vanishes and the original one is re-created. Since counting rearrangements as numbers does not take into account the directions of junctions, a rearrangement plus its opposite are counted as $1 + 1 = 2$ rearrangements, although their total effect does not contribute to tissue morphogenesis. Conversely, Butler *et al.* (49) used their own method (defined in ref. (30)). They computed the contribution of cell shape change to flow. They then subtracted the cell shape change rate from the tissue shape change rate. They thus indirectly inferred the correct contribution of rearrangements to morphogenesis as matrices, *i.e.* including their amplitude but also their direction.

Here, to characterize cell dynamics in term of cell shape changes and cell rearrangements, we applied to tissue morphogenesis a formalism based on texture, validated on foam dynamics (46). Overall, 10 wt, 5 $dachs^{RNAi}$, 5 ds^{RNAi}, 4 fat^{RNAi} and 2 ft^{UP} movies at 29°C were segmented and analyzed in the interval 17:20 - 21:20 hAPF. For each IC-box, we listed the cells i which centroid was in this box at time t. The total texture M of these cells was defined as (Eq. 6 of ref. (46)):

$$M(t) = \sum_i \frac{1}{2} \sum_j w_{ij} m_{ij}. \tag{17}$$

Here j labels each neighbor of cell i, the vector $\vec{\ell}_{ij} = (X_{ij}, Y_{ij})$ is the link between the centers of cells i and j, the factor 1/2 avoids counting twice each link, the weight w_{ij} is 1 for all normal links and 1/2 for the few links belonging to a 4-fold vertex, and m_{ij} is the tensorial (or outer) product of $\vec{\ell}_{ij}$ by itself:

$$m_{ij} = \vec{\ell}_{ij} \otimes \vec{\ell}_{ij} = \begin{pmatrix} X_{ij}^2 & X_{ij}Y_{ij} \\ X_{ij}Y_{ij} & Y_{ij}^2 \end{pmatrix} \tag{18}$$

The texture thus expresses the variance of link length in all directions. The cumulative variation of texture over these 4 hours under consideration, $\Delta M = M(t + 4\text{h}) - M(t)$, was calculated in each IC-box.

Cell shape changes in each IC-box were defined as the rate of texture variation, $\Delta M/4\text{h}$, and expressed in μm^2 min^{-1} (Eq. C3 in appendix of ref. (46)). Cell shape changes were measured as matrices, in order

to retain information regarding their direction and anisotropy, relevant to characterize contributions to tissue shape change. In what follows we do not use their trace, related to changes in cell sizes. They were represented as cyan bars along the direction of cell contractions (fig. S13A).

Cell rearrangements too were directly measured as matrices in the same formalism and expressed in the same units, namely μm^2 min^{-1} (Eq. 11 of ref. (46)). In each IC-box, at time t, we listed cells i which centroid was in this box at two successive images t, $t+\delta t$ and did not divide during δt. The total rearrangement rate of these cells was measured as $R(4\text{h})/4\text{h}$ where $R(4\text{h})$ was the sum of rearrangements at each time interval δt, defined as follows:

$$R(\delta t) = \sum_i \frac{1}{2}\left(-\sum_{j^\ell} w_{ij}m_{ij} + \sum_{j^g} w_{ij}m_{ij}\right). \tag{19}$$

Here the sums are taken on links j^ℓ which are lost during δt, that is, cells which were neighbors of i at t but no longer at $t+\delta t$ (yellow lines in Movie S2C,C'): they contribute negatively. Similarly, links j^g which are gained during δt, that is, cells which become neighbors of i at $t+\delta t$ (red lines in Movie S2C,C') contribute positively. They were represented as red bars along the direction of gained center-center links, thus in the direction of lost cell-cell junctions (fig. S13B). If two cells transiently lose their junction, then regain it, their link disappears then re-appears, and the total contribution of such back-and-forth rearrangement to the rearrangement matrix is close to zero, as it should be. When a four-fold vertex was detected during a rearrangement, the corresponding links (shown in lighter colours in Movie S2C,C') were counted with a weight 1/2 so that the total contribution of the corresponding rearrangement was independent of the detection of the four-fold vertex.

Using movie registration in time and space, measurements were averaged over several movies, thus providing a good signal to noise ratio. This enabled us to use our subtractive method (section 3.2.1) to calculate the local differences in cell rearrangements and cell shape changes in wt and mutant conditions that contribute to the differences in local tissue contraction rates. This led to the determination of the specific Dachs polarization contributions to cell rearrangements or to cell shape changes. In turn, these contributions were correlated with the differences in tissue contraction rates over regions of strong D:GFP polarization. The mutual alignment coefficient A of cell shape changes and contraction rate, or rearrangement rate and contraction rate, was plotted in the spirit of section 3.3.2, without weights, at places where the FT pattern $\overline{\overline{\mathbf{Q}}}$ was significant (purple in Fig. 4E'F', fig. S15A"B", fig. S16E'-H').

5 Supporting figures and movies

5.1 Supporting figures

In all figures, the positions of the macrochaetae and of the midline are indicated by yellow circles and by a cyan dashed line, respectively. Data on flow, FT and division are averaged over 64×64 pixels squares ($\sim$ 20×20 μm^2) and 24 interframes (2 h). Such space and time intervals are large enough to yield a signal to noise ratio suitable for the analyses presented here, and small enough to observe relevant details in morphogenetic movements.

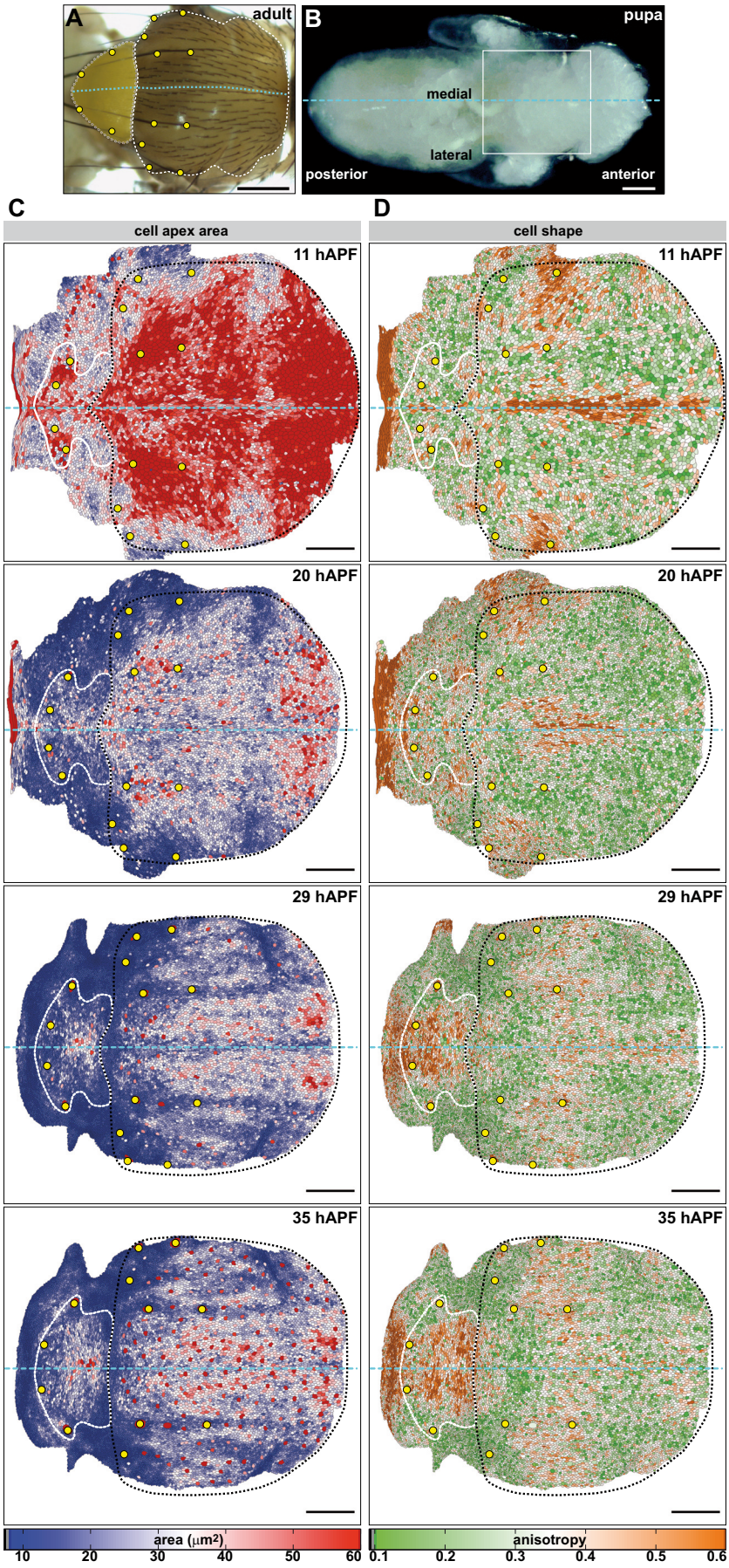
A
adult
B
pupa
medial
lateral
posterior
anterior
C
cell apex area
D
cell shape
11 hAPF
20 hAPF
29 hAPF
35 hAPF
area (μm²)
10
20
30
40
50
60
anisotropy
0.1
0.2
0.3
0.4
0.5
0.6

Figure S1. Metamorphosis of the *Drosophila* dorsal thorax. *The visible symmetry of the patterns with respect to the midline underlines that they are finely regulated at the scale of 10-20 cell clusters rather than at the individual cell level. Using Gaussian filters of increasing sizes confirms that these patterns become completely symmetric when blurred above 10-20 cell sizes.*

(**A**) *Drosophila* adult dorsal thorax. The visible part of the adult scutellum is shaded in yellow and the scutum is outlined by a white dashed line. (**B**) Dorsal view of the *Drosophila* pupa without pupal case, here at 14 hAPF. The white box indicates the position of the thorax. (**C-D**) Cell-level measurements at 11, 20, 29 and 35 hAPF during morphogenesis of the pupa dorsal thorax. (C) Cell apex area, in color code scale from blue (10 μm^2) to red (60 μm^2). (D) Cell shape anisotropy, defined as one minus the ratio between the minor to major axes of the best fitting ellipse, from green (0.1) to brown (0.6). The scutellum is outlined by a white dashed line, the scutum by a black one. Scale bars: 250 μm (A, B), 100 μm (C, D).

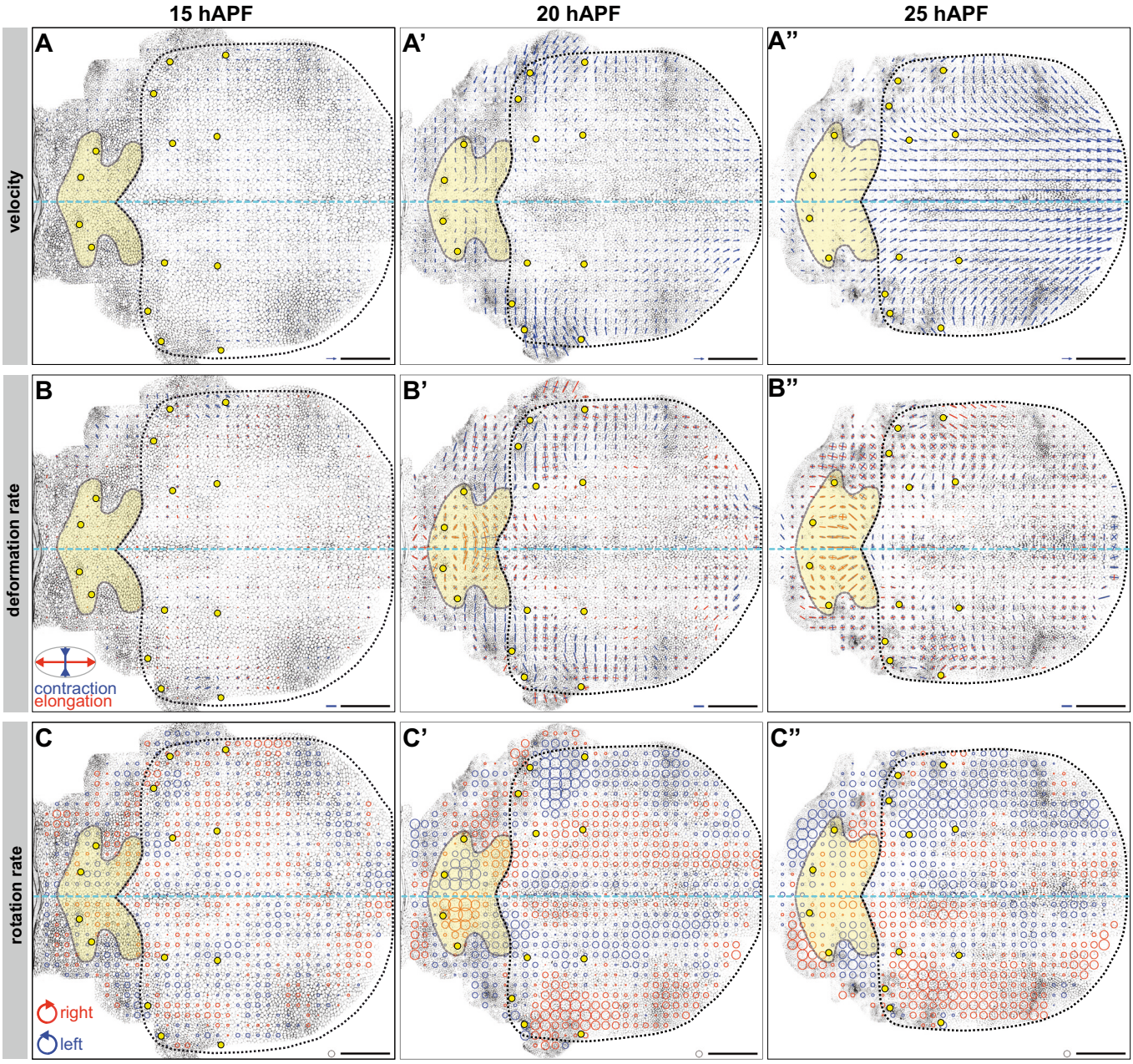

Figure S2. Tissue dynamics in the pupa dorsal thorax during metamorphosis. *These maps are representative of the three main phases of dorsal thorax development. (i) From 14 to 17 hAPF, no major morphogenetic movement is observed (A, B), yet epithelial cells of the dorsal thorax undergo a first round of division (fig. S12B and Movies S1, S2). The tissue undergoes only small local rotation (C). (ii) From 17 to 21 hAPF, a symmetric lateral to medial flow is observed within the lateral domain of the dorsal thorax (A'), corresponding to the contraction of the lateral domains of the dorsal thorax (B') and its anterior-posterior elongation (B' and Movie S3). This flow is associated with cell apical constriction in the lateral domain of the scutellum (compare the 11 h and 20 h panels of Fig. S1C). Concomitantly, a medial to lateral flow is observed in the scutellum (A'), corresponding to the contraction-elongation of its medial domain (B') and its dorsal-ventral elongation (B' and Movie S3). During this period, extensive rotation is observed in the dorsal*

thorax (C'). (iii) From 21 to 36 hAPF, a symmetric lateral to medial flow and a major posterior to anterior flow are observed in the scutum (A"). These flow are associated with contraction-elongation deformation of its lateral domains (B") and its anterior-posterior elongation, as well as with the contraction of the pupa neck region. During this period the scutellum mostly expands in all directions (B"). High tissue rotation rates are observed in the lateral domain of dorsal thorax (C").

(**A-C")** Maps at 15 (A-C), 20 (A'-C') and 25 (A"-C") hAPF. (A-A") local velocities represented as vectors. (B-B") Deformation rates represented as ellipses: a direction of elongation is represented in red and contraction in blue. (C-C") Rotation rate represented by circle diameters: clockwise is represented in red and counter-clockwise. The scutellum is shaded in yellow and the scutum is outlined by a black dashed line. Scale bars: 100 μm (black bars), 9×10^{-2} μm min^{-1} (arrows in A-A"), 2.4×10^{-3} min^{-1} (blue bars in B-B"), 8×10^{-5} min^{-1} (circles in C-C").

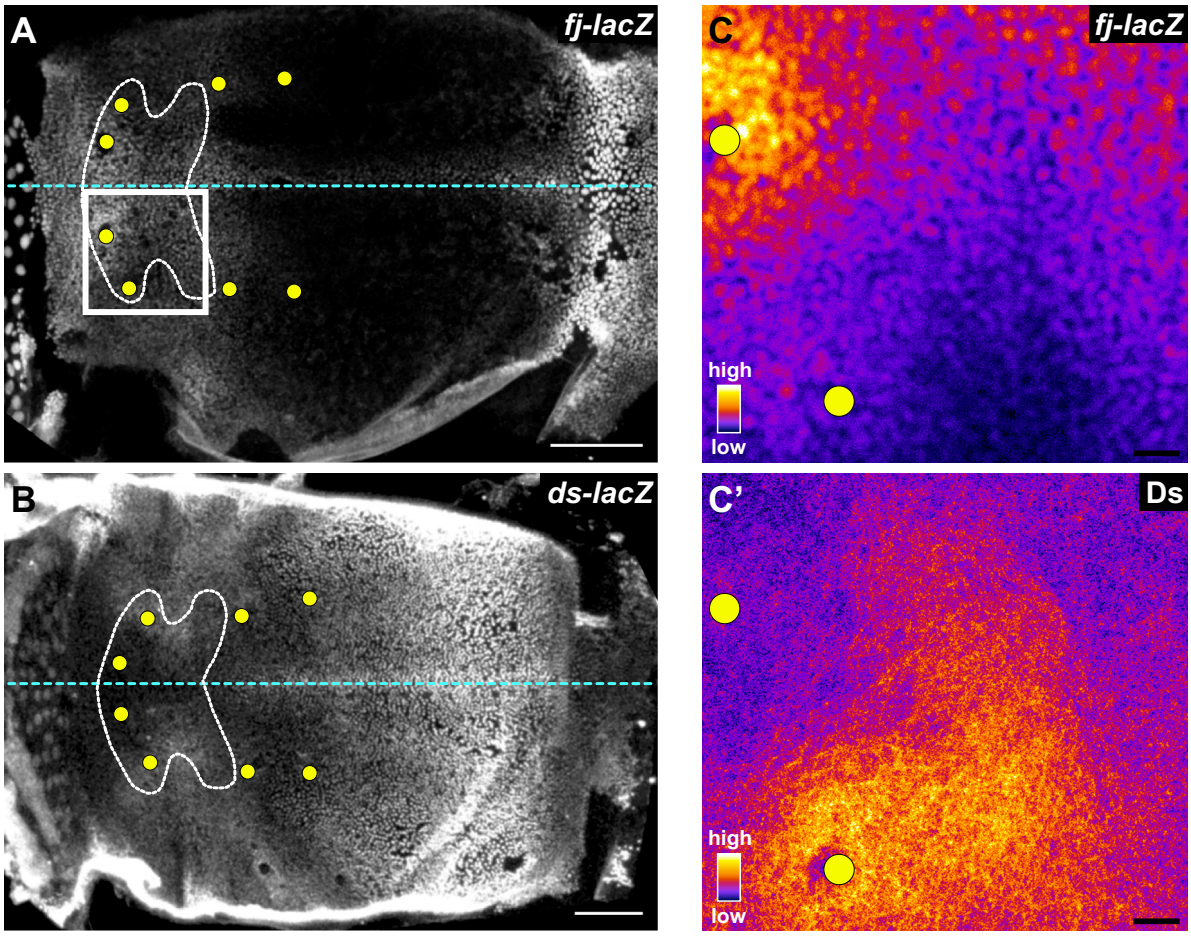

Figure S3. Gradients of *fj* and *ds* expressions are opposed in the scutellum. *Whereas ds had an elaborate expression in the dorsal thorax, fj was mostly expressed in the medial domain of scutellum. Hence fj and ds are expressed in opposing domains in the scutellum and in the most posterior part of the scutum.*

Anti-βgal staining of (**A**) *fj-lacZ* and (**B**) *ds-lacZ* in the pupa dorsal thorax at 19 hAPF. The scutellum is outlined by a white dashed line. (**C,C'**) Average patterns (n = 7 pupae) of *fj-lacZ* (C) and Ds (C') determined in the region marked in A by a white box. Scale bars: 100 μm (A,B), 10 μm (C,C'), .

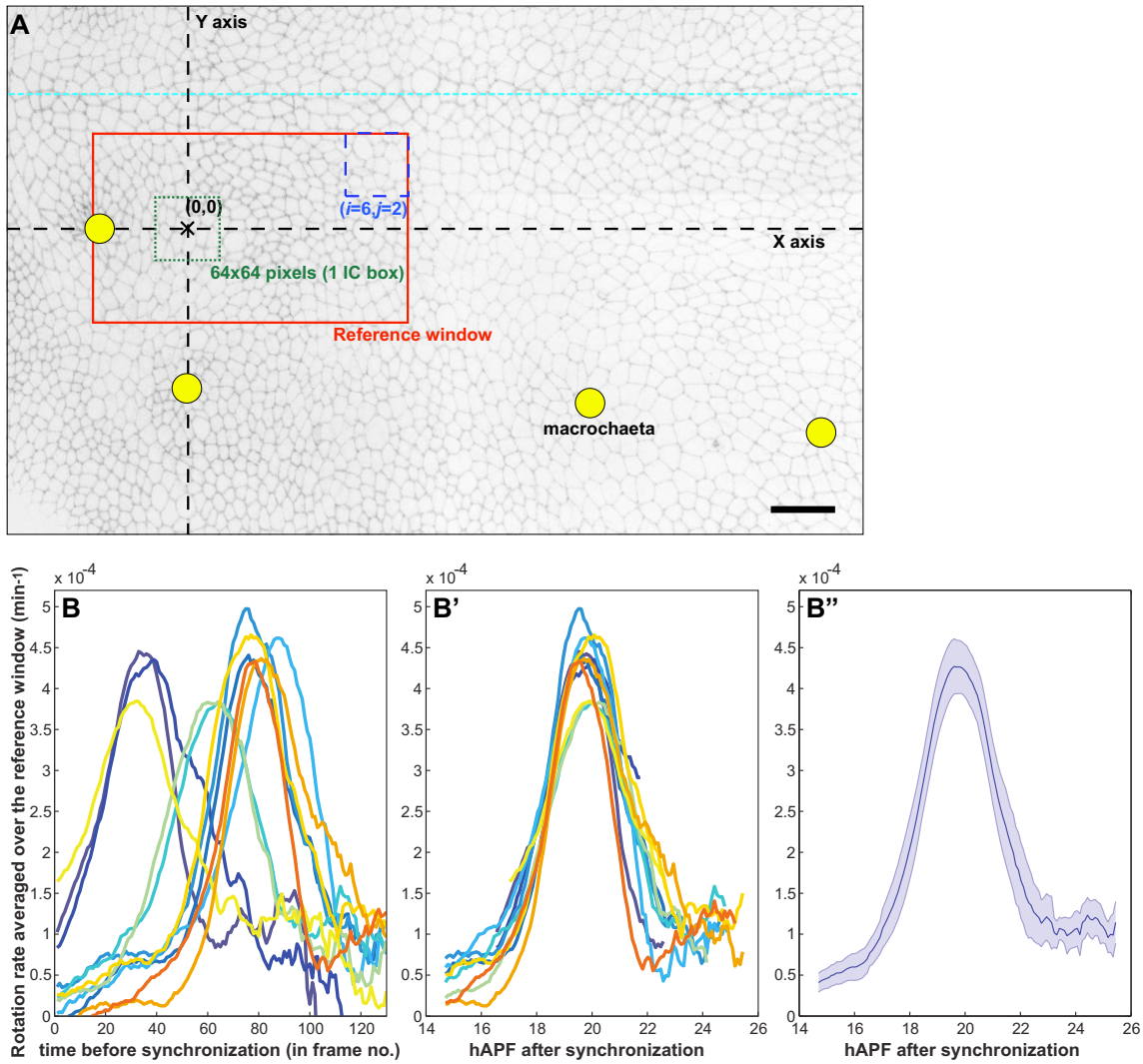

Figure S4. Spatio-temporal registration of movies. *In order to compare different hemi-scutellum movies corresponding to the same genotype, and/or average their measurements to improve the signal to noise ratio, their common space and time coordinates were defined in two steps: first, spatial registration of the IC grid using the positions of the two scutellar macrochaetae (A); second, time registration using the point with the steepest slope before the rotation rate peak (B-B").*

(**A**) Image of a wt hemi-scutellum at 16:30 hAPF showing the landmarks used for spatial adjustment between movies. The X and Y axes were determined using the positions of the macrochaetae at 16:30 hAPF. Red rectangle (IC-boxes labelled $i = -2$ to 6 and $j = -2$ to 2): window over which the rotation rate was measured and spatially integrated, called "reference window". Two IC-boxes are shown as dashed squares with their space coordinates (i, j) indicated. (**B-B"**) Synchronization: graphs showing the rotation rate of 11 wt movies at 29°C calculated in the reference window defined in A: (B) before and (B') after synchronization using as a reference 3/4 of the rotation peak in the ascent (set to 18:40 hAPF). (**B"**) Graph showing the average rotation rate ± SD of the same 11 wt movies after space and time registrations. Scale bar: 20 μm (A).

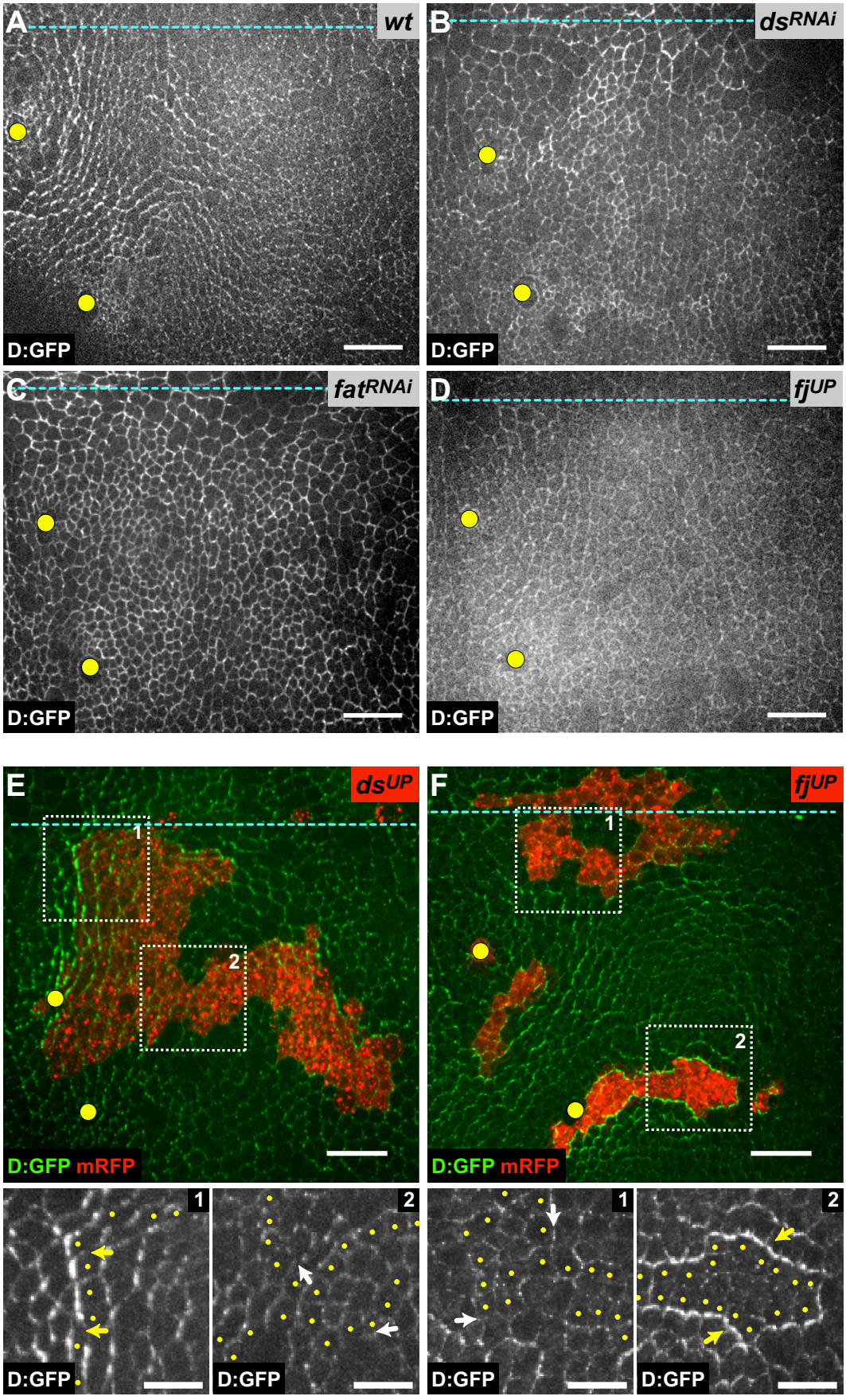
A
wt
D:GFP
B
dsRNAi
D:GFP
C
fatRNAi
D:GFP
D
fjUP
D:GFP
E
dsUP
1
2
D:GFP mRFP
F
fjUP
1
2
D:GFP mRFP
1
D:GFP
2
D:GFP
1
D:GFP
2
D:GFP

Figure S5. Regulation of Dachs polarization *D:GFP planar polarity lines (A) are lost when the Ds gradient is eliminated (B), Fat activity is abolished (C) or the Fj gradient is flattened (D). Furthermore, creation of ectopic Ds-Fj gradient boundaries by overexpression of either Ds (E) or Fj (F) polarizes D:GFP towards the highest concentration of Fj.*

(**A-D**) Localization of D:GFP in wt (A), ds^{RNAi} (B), fat^{RNAi} (C) and fj^{UP} (D) scutella. **(E)** Localization of D:GFP (green, gray in close-ups) in wt cells and in cells overexpressing *ds* (ds^{UP} cells marked by mRFP expression, red). Close-ups in regions 1 and 2 show that *ds* overexpression polarizes D:GFP in region 1 (yellow arrows), where *fj* is highly expressed, but not in region 2 (white arrows) where *fj* expression is low. Yellow dots indicate ds^{UP} cells abutting the wt cells. **(F)** Localization of D:GFP (green, gray in close-ups) in wt cells and in cells overexpressing *fj* (fj^{UP} cells marked by mRFP expression, red). Close-ups in regions 1 and 2 show that *fj* overexpression polarizes D:GFP in region 2 (yellow arrows), where *ds* is highly expressed, but not in region 1 (white arrows) where *ds* expression is low. Yellow dots indicate fj^{UP} cells abutting the wt cells. Scale bars: 20 μm (A-F), 10 μm (close-ups of E,F).

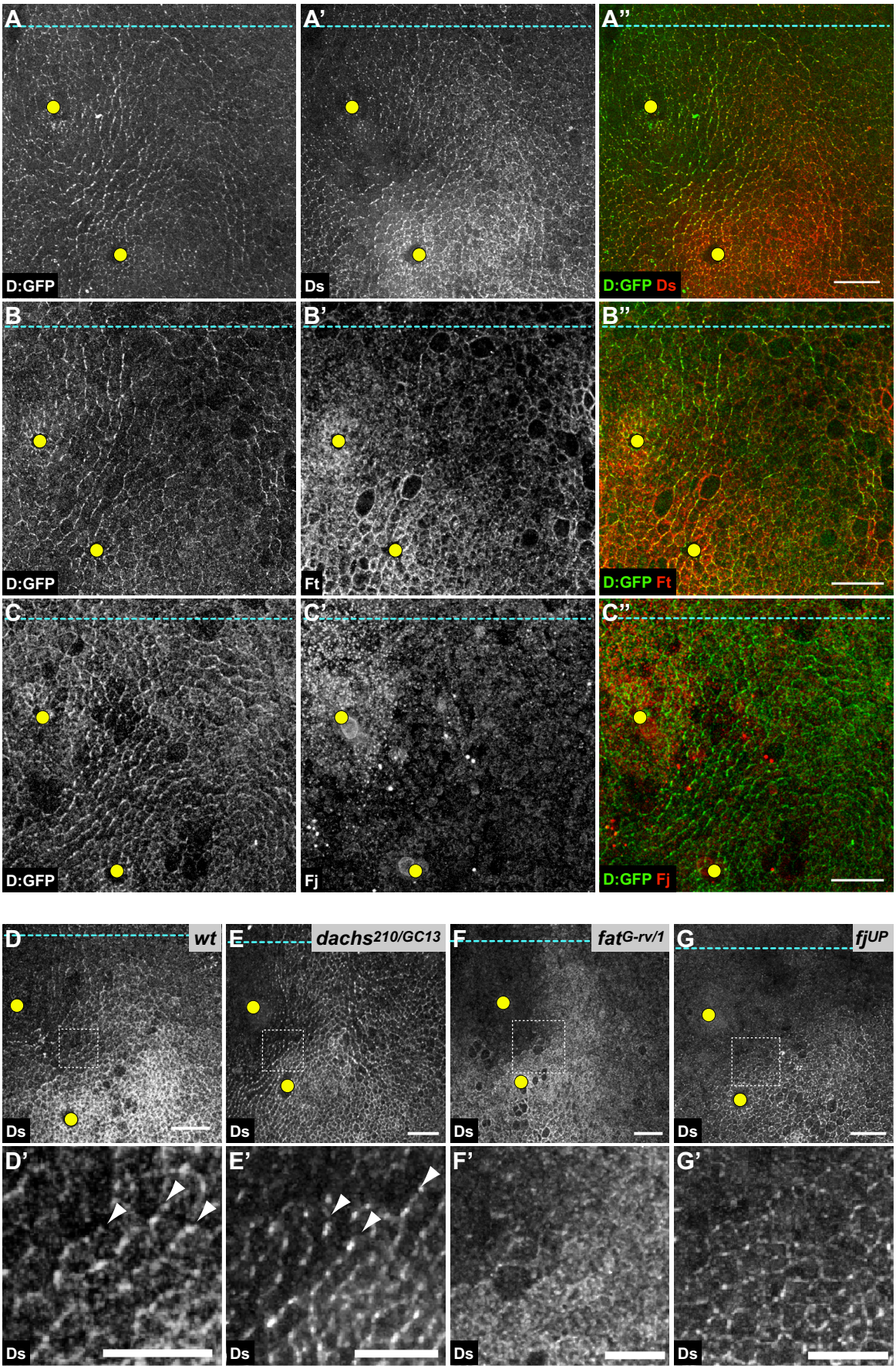
A
A'
A"
D:GFP
Ds
D:GFP Ds
B
B'
B"
D:GFP
Ft
D:GFP Ft
C
C'
C"
D:GFP
Fj
D:GFP Fj
D
wt
E
dachs210/GC13
F
fatG-rv/1
G
fjUP
Ds
D'
E'
F'
G'

Figure S6. Ds planar polarization is independent of Dachs activity, but requires Fat activity as well as the graded distribution of Fj. *Fat is enriched in some regions of the scutellum but is not as clearly polarized as Ds (compare A-A" and B-B"). Fj is mostly localized in domains corresponding to the ones detected by fj-lacZ reporter (Fig. 2A and fig. S3C). Fj accumulates in small intracellular punctuated structures as expected for a Golgi resident protein. Ds is normally polarized in* $dachs^{210/GC13}$ *tissue. In* $fat^{G-rv/1}$ *and* fj^{UP} *pupae, Ds remains at the cell membrane, but Ds polarization is hardly detectable.*

(**A-A"**) Localization of D:GFP (white in A, green in A") and Ds (white in A', red in A") in the scutellum. (**B-B"**) Same for Fat. (**C-C"**) Same for Fj. **(D-G')** Localization of Ds in wt (D,D'), $dachs^{210/GC13}$ (E,E') and $fat^{G-rv/1}$ (F,F') scutella, and in Fj overexpressing fj^{UP} (G,G') scutellum. D'-G' are close-ups of the regions outlined in D-G, respectively. Scale bars: 20 μm (A-G), 10 μm (D'-G').

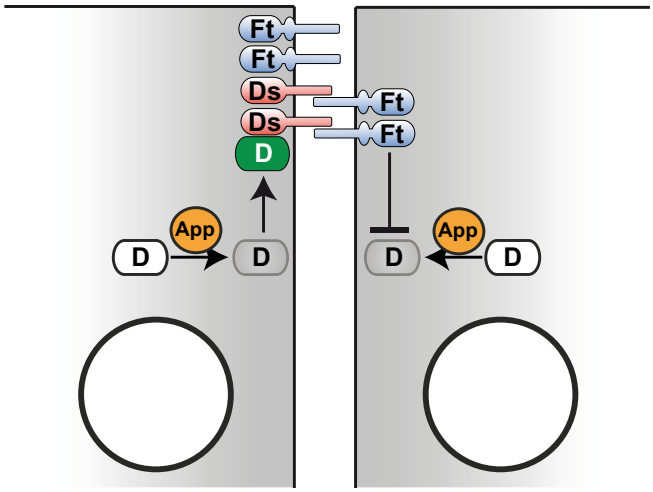

Figure S7. Regulation of Dachs asymmetric membrane localisation. Schematic: thin line, cell membrane; thick line, nucleus. Genetic evidences show that Fat activity inhibits Dachs membrane localisation (6, 50), whereas the DHHC Palmitoyltransferase Approximated (App) enzyme promotes Dachs membrane localisation (51). Fat and App are homogeneously distributed at the cell membrane (21, 51, 52). Our results showing that Ds is asymmetrically distributed and that Ds can interact with Dachs permit to propose that upon localisation of Dachs at the membrane by App, Ds polarizes Dachs distribution by two complementary mechanisms: (i) in an autonomous manner, Ds promotes Dachs asymmetric distribution by interacting with Dachs; (ii) in a non-autonomous manner, Ds polarizes Fat signalling in the neighboring cell, thereby excluding Dachs from the cell membrane facing the one where Ds is enriched. Fat processing and phosphorylation (not depicted) might contribute to the polarization of Fat activity in response to Ds binding (**? ?**).

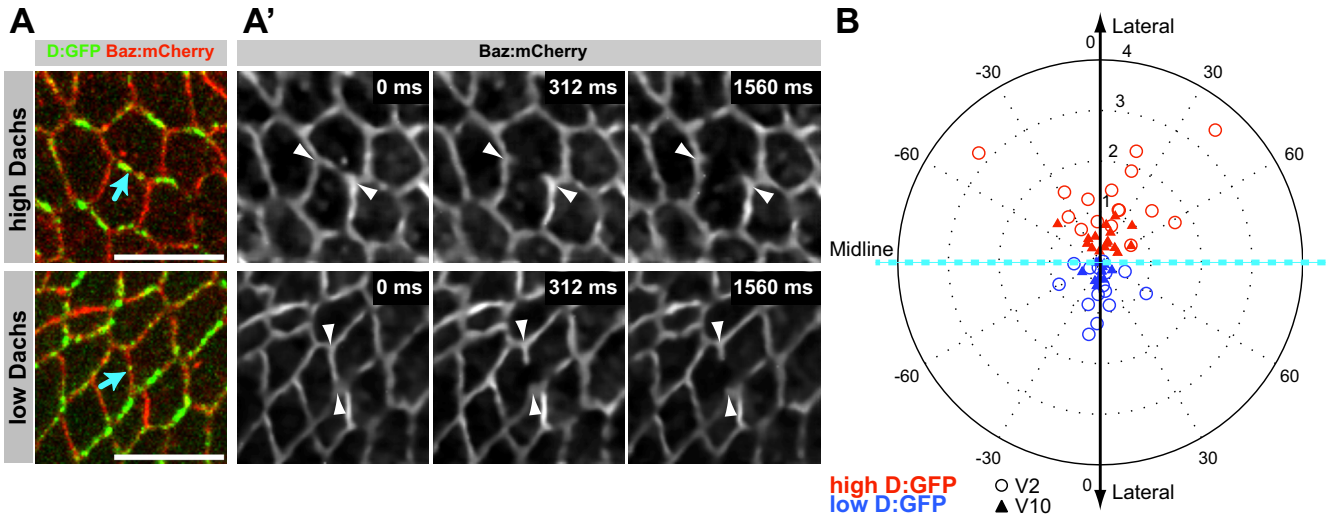

Figure S8. Cell junction tension correlates with Dachs enrichment and not with junction orientation. *The D:GFP enriched junctions can be found at various orientations relative to the anterior-posterior animal axis (Fig. 4A) and we have ablated an unbiased sample. We find that the amplitude of relaxation speed, and thus the amplitude of the tension, does not correlate with the direction of the junction prior to ablation: p-values determined using the circular-linear correlation defined in Eq 27.47 of (53) and in (54) were larger than 0.05 (for high, low or all D:GFP levels they were p =0.32, 0.22 and 0.31, respectively). We interpret this absence of correlation by stating that the junction tension depends on its level of Dachs, while it does not depend on its orientation.*

(**A**) Cell junctions with high or low D:GFP (arrows) 1560 ms prior to ablation. (**A'**) Images of Bazooka:mCherry prior to and following ablation (see Movie S5). Arrowheads indicate the position of vertices. (**B**) Plot of the initial relaxation speed (μm s^{-1}) of vertices after ablation of cell junction with high (red) or low (blue) D:GFP levels, versus direction of the junction prior to ablation, plotted in two symmetrical hemicircles for clarity. Circles are V_2 and triangles are V_{10} (see section 1.6.2 for details). Scale bars: 10 μm.

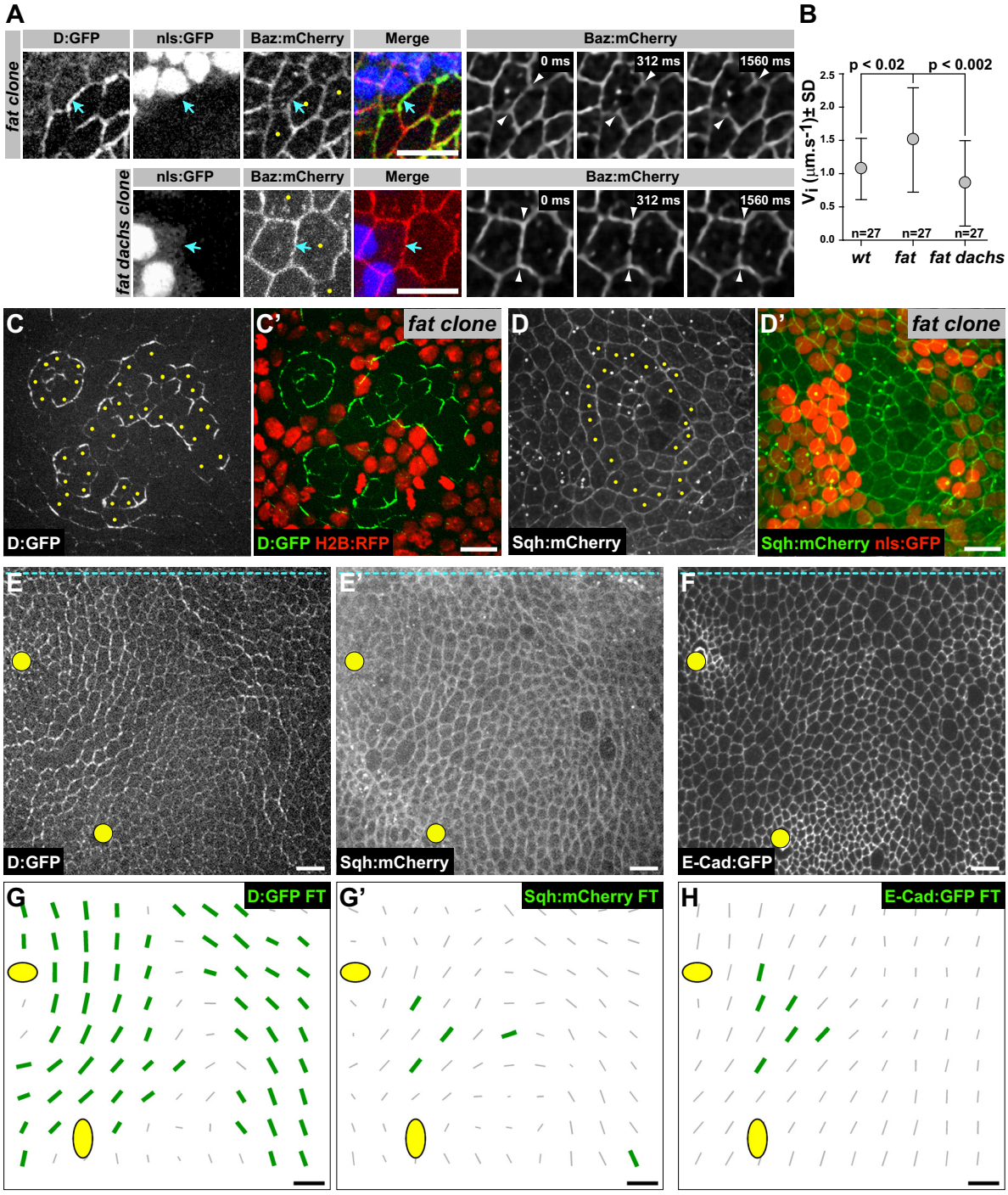

Figure S9. Regulation of tension anisotropy by Dachs polarization independently of MyosinII polarization. *To assess whether Dachs regulates junction tension anisotropy independently of MyosinII polarization we performed several experiments. First we measured cell junction tension at the border between mutant and wt cells using laser ablation in mosaic tissues. It is established that fat clones trigger Dachs polarization at the interface between wt and fat mutant cells (6, 50). The interface between wt and mutant cells therefore provides an artificial boundary to analyse the role of Dachs polarization in junction tension by comparing the tension between wt and fat junctions and wt and fat, dachs double mutant junctions*

(A). Our ablation experiments revealed that indeed these ectopic cell junctions enriched in Dachs exhibited Dachs-dependent increase in cell junction tension (B). Furthermore, the interface between wt and fat cells does not show MyosinII polarization, as shown by Drosophila Myosin light chain (Spaghetti squash, Sqh) localization (compare C and D). Finally, we have simultaneously recorded D:GFP and Sqh:mCherry during scutellum morphogenesis (E,E'). The quantification of their anisotropy by FT demonstrated that D:GFP is strongly and significantly polarized within the scutellum whereas Sqh:mCherry is not (G,G'). For comparison we also performed identical analyses on E-Cad:GFP movies during scutellum morphogenesis and found a nearly identical polarization pattern as we observed for the Sqh:mCherry (H). Both the Sqh:mCherry and E-Cad:GFP patterns were just below or just above the threshold at few places where cells are much elongated. Everywhere else, they are not significantly different from zero. Combined, these results demonstrate that Dachs polarization results in anisotropic interfacial tension. The molecular mechanism of how Dachs generates tension remains to be characterized. However, Dachs is most closely related to the well characterized MyosinV and MyosinI (55) which have been shown to produce movement on actin using in vitro assays (56, 57). Furthermore, sequence analyses of Dachs demonstrated that all the necessary domains to be an actin motor (actin bindings site, nucleotide binding domain), and hence to produce force, are present (A. Houdusse, personal communication). Dachs mostly differs from MyosinV or I in the transducer domain, which determines the processivity of the myosin motor. Based on the sequence comparison of Dachs with MyosinV or MyosinI, which have been crystallized and biochemically characterized (58, 59), the most likely scenario is that the interfacial tension is generated by the contractile force generated by the motor activity of the Myosin Dachs in complex with proto-cadherin Dachsous.

(A) Representative images of cell junction ablation between wt and *fat* cells (upper panels) and between wt and *fat dachs* cells (lower panels) prior to ablation and after ablation (top right corner of each panel indicates the time relative to ablation). Mutant cells are marked by the absence of nls:GFP. Yellow dots indicate mutant cells abutting wt cells. Arrows indicate the ablated junctions and arrowheads the position of the vertices. Cell junctions between wt and *fat* cells have increased amounts of D:GFP (first panel and see also C). Ablations at junctions between wt and *fat* cells and control ablations (between differently marked wt cells) were performed in pupae expressing both D:GFP and Baz:mCherry, while ablations of junctions between wt and *fat dachs* cells were performed in pupae that expressed only Baz:mCherry. All ablations have been performed in the scutum to avoid the endogenous polarization of Dachs. **(B)** Graph of the mean initial relaxation speeds of vertices in junctions between wt and wt cells (1.07 ± 0.46 μm s^{-1}, $n = 27$), wt and *fat* mutant cells (1.50 ± 0.78 μm s^{-1}, $n = 27$) and wt and *fat dachs* double mutant cells (0.85 ± 0.64 μm s^{-1}, $n = 27$). **(C,C')** D:GFP (grey in C and green in C') in wt and *fat* cells. Mutant cells are marked by the absence of H2B:RFP (red in C'). D:GFP is enriched at the interface between wt and *fat* cells. **(D,D')** Sqh:mCherry (grey in D and green in D') in wt and *fat* cells. Mutant cells are marked by the absence of nls:GFP (red in D'). No polarization of Sqh:mCherry can be detected at the interface between wt and *fat* cells. **(E,E')** Images of the scutellum at 19 hAPF of a pupa expressing D:GFP (E) and Sqh:mCherry (E'). **(F)** E-Cad:GFP in the scutellum at 19 hAPF. **(G,G',H)** FT analyses of E,E',F averaged between 17:20 and 21:20 hAPF ($n = 3$ for each panel): maps of the D:GFP (G), Sqh:mCherry (G') and E-Cad:GFP (H) anisotropy. Significant data: green bars; other: gray bars. In all panels, yellow dots indicate mutant cells abutting wt cells. Scale bars: 10 μm.

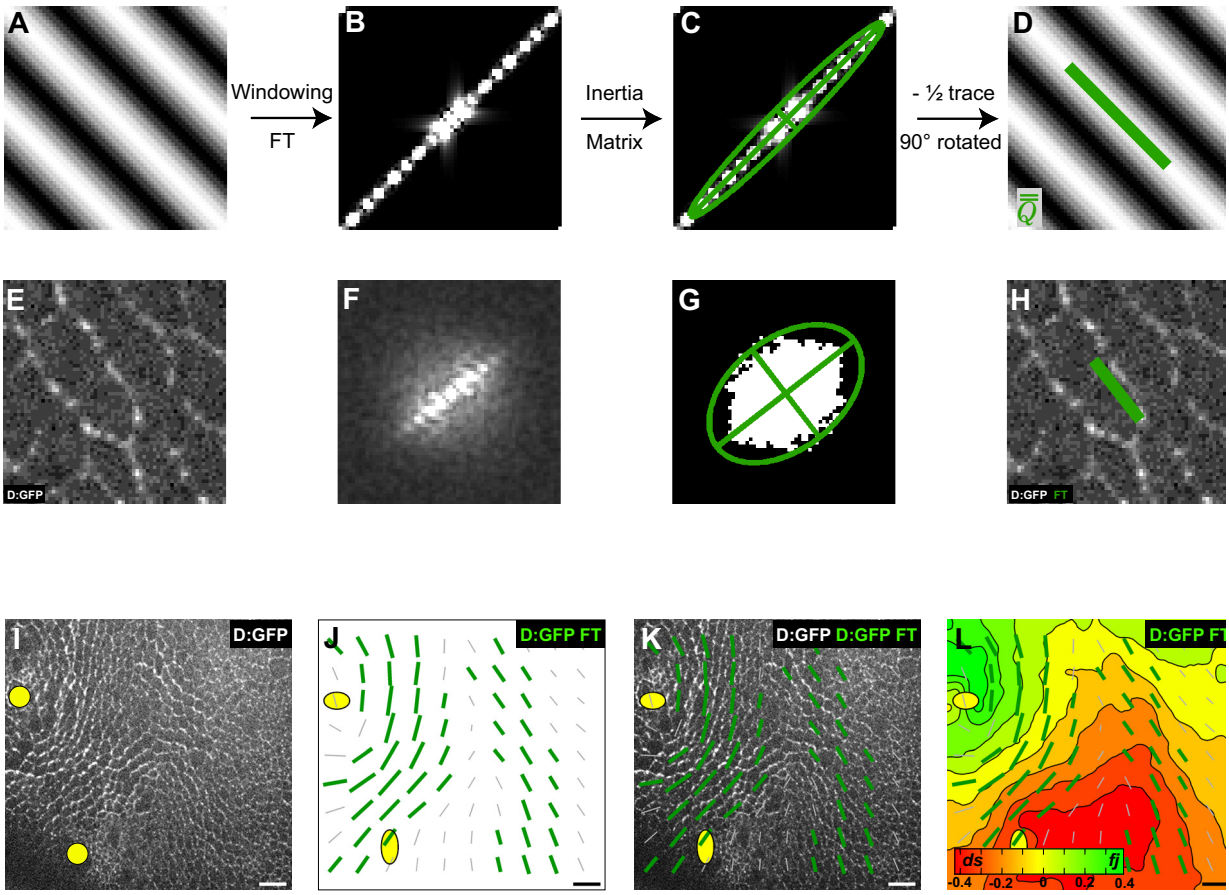

Figure S10. Quantification of D:GFP pattern anisotropy. *A green bar is plotted in the direction of D:GFP pattern anisotropy, quantified by 2D discrete Fourier transform (FT) analysis used to build the* $\overline{\overline{\mathbf{Q}}}$ *matrix (section 2.3.3). It correlates with the position and shape of the opposing fj and ds gradients pattern.*

(A-D) FT and construction of $\overline{\overline{\mathbf{Q}}}$ on a basic example. (A) Periodic sinusoidal pattern tilted at 45°. (B) FT norm of image A represented in the Fourier space, after an appropriate windowing (multiplication by a square cosine) that minimizes the edge effects. The origin of the Fourier space has been shifted so that it is at the center of the panel in the Fourier space, rather than in a corner. (C) Inertia matrix of the pixels in B that are above the 80^{th} percentile, represented as a green ellipse and overlayed to B. (D) The matrix obtained in C has its trace removed (half trace subtracted from each diagonal term), the square root of its positive eigenvalue is represented after 90° rotation and multiplication by the contrast of A (here equal to 1). The resulting green bar represents $\overline{\overline{\mathbf{Q}}}$ which quantifies the anisotropy and orientation of the pattern visible in A. **(E-H)** FT and construction of $\overline{\overline{\mathbf{Q}}}$ for an actual Dachs signal. (E) Raw image extracted from a time-lapse D:GFP movie, cropped in an IC-box.(F) Same as B, averaged over 2 h. (G) Same as C. (H) Same as D. **(I-L)** Pattern of D:GFP polarization. (I) Snapshot of D:GFP pattern. (J) Map of the D:GFP magnitude and anisotropy determined by Fourier Transform (FT) on the average of D:GFP time-lapse movies ($n = 3$) between 17:20 and 21:20 hAPF. Significant data: thick green bars; other: thin gray bars. (K) Overlay of (I) and (J). (L) Overlay of (J) and fig. 2A. Box size: 64×64 pixels $\sim 20 \times 20$ μm^2 (A,D,E,H). Scale bars: 10 μm (I-L).

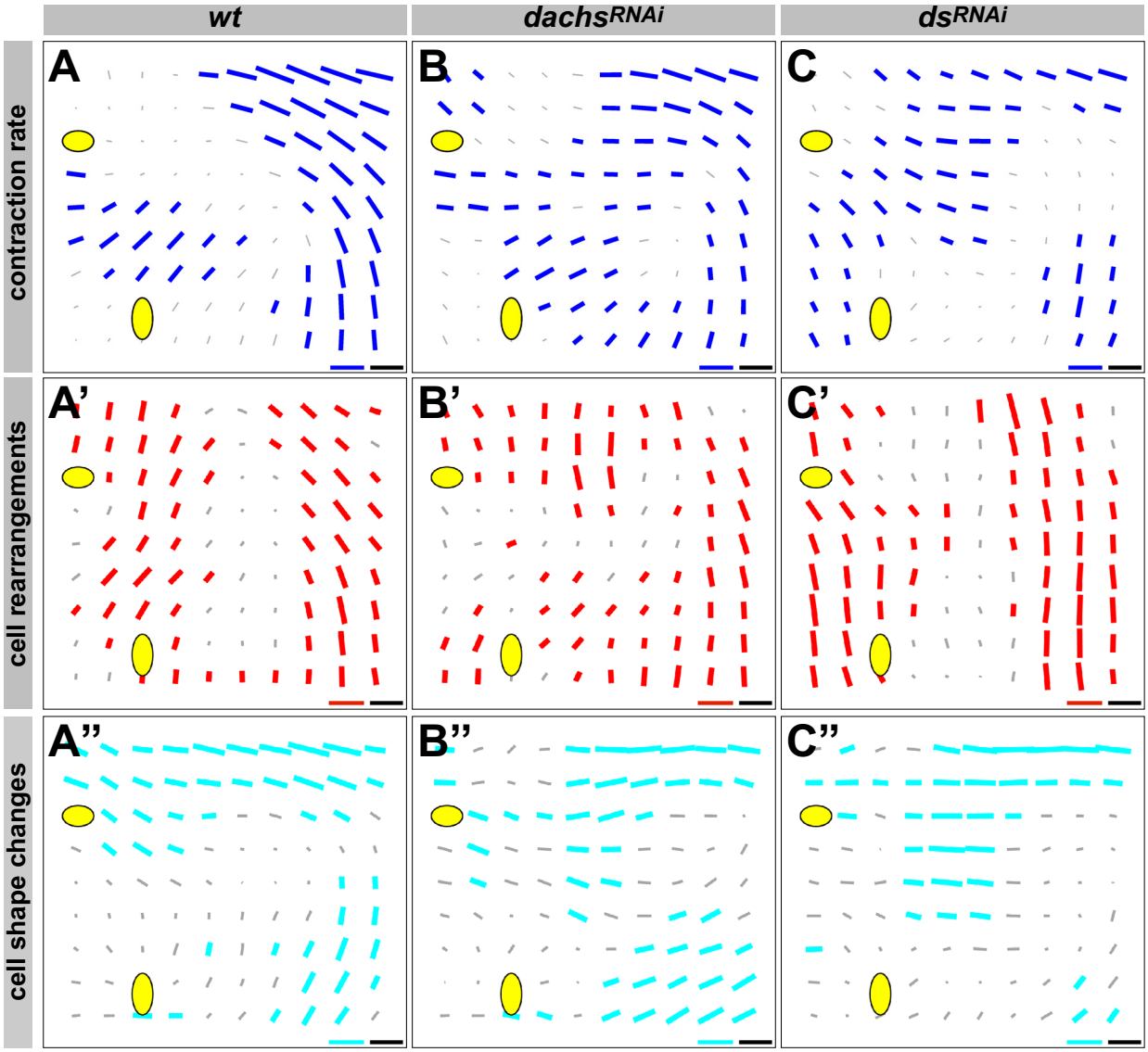

Figure S11. Contraction rates, cell rearrangements and cell shape changes in wt, *dachs*^{RNAi} and *ds*^{RNAi} hemi-scutella. *Having observed similarities between the wt contraction rate map (A) and the Dachs signal pattern (Fig. 4A), we looked for the specific contribution to flow of Dachs and Ds (other mutations of the Fat/Ds/Fj pathway are presented in fig. S16). The flow in wt, dachs*^{RNAi} *and ds*^{RNAi} *tissues was calculated according to the right hand side of Eq. (11). Using the flow presented here (B-C), we subtracted the contraction rates of dachs*^{RNAi} *from wt (A-B), and of ds*^{RNAi} *from wt (A-C), according to Eq. (11). This yielded the maps presented in Fig. 4C,D. We then used the method explained in section 4.2 to measure the contributions of cell rearrangements (A'-C'), and of cell shape changes (A"-C") to tissue contraction. They too are represented as bars, as explained in fig. S13.*

(**A-C"**) Maps of local contraction rate $\overline{\overline{\nabla \mathbf{V}}}^{dev}$ (A-C), traceless parts of rearrangement matrix (A'-C') and of cell shape change matrix (A"-C") between 17:20 and 21:20 hAPF in wt(A-A"), *dachs*^{RNAi}(B-B"), and *ds*^{RNAi}(C-C") scutella. Significant values are shown as thick colored bars, others are shown as thin gray bars. Yellow ellipses indicate the ensemble average ± SD positions of the macrochaetae. Scale bars: 10 μm (black bars); 5.5×10^{-4} min^{-1} (blue bars in A-C); 1 μm^2 min^{-1} (red bars in A'-C', cyan bars in A"-C").

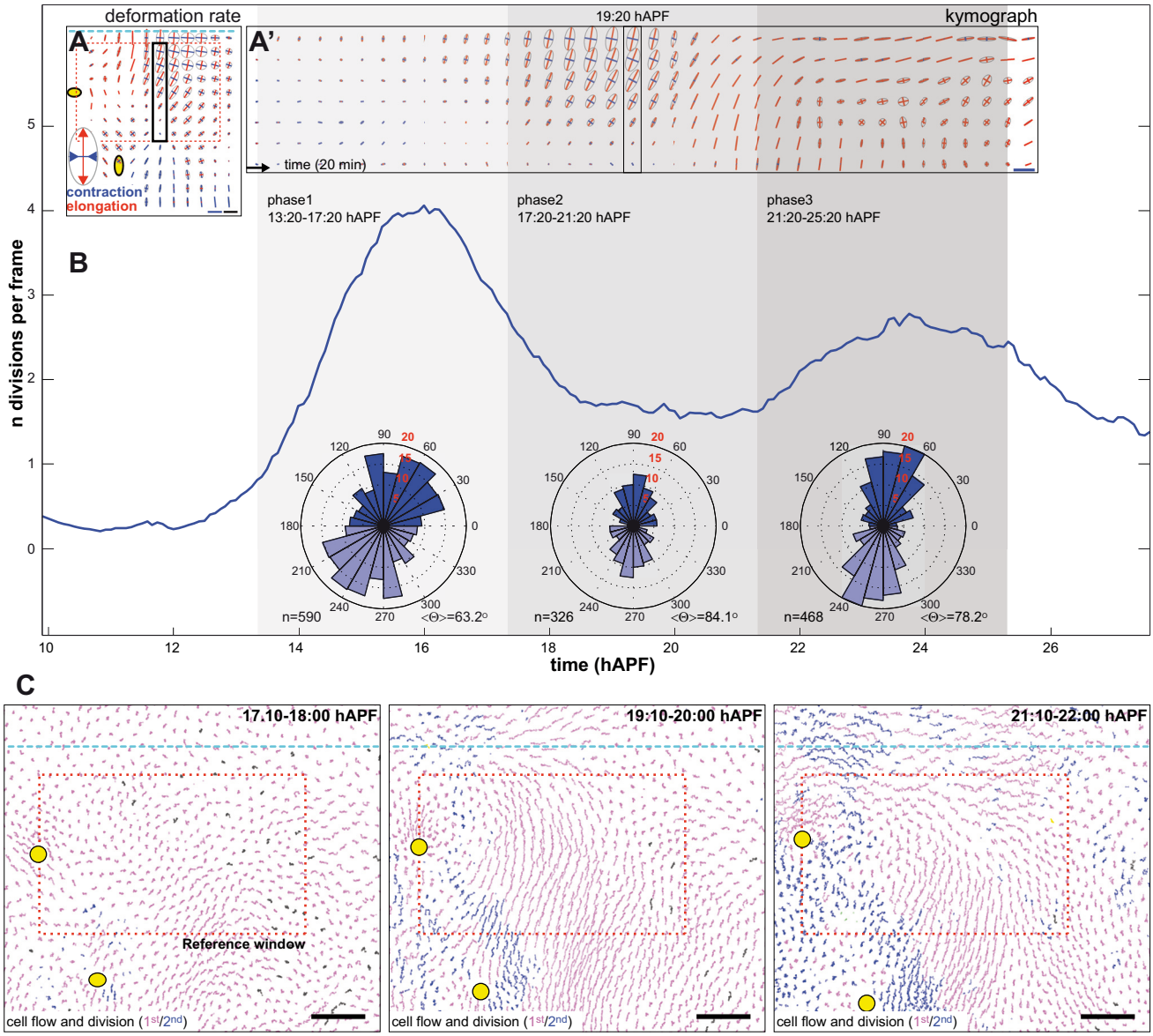

Figure S12. Contraction-elongation of the scutellum medial region does not correlate with cell divisions. *To investigate the role of cell division orientation in scutellum morphogenesis, we have first compared the magnitude of tissue deformation with the timing and the orientation of cell division (A, A' and B). Second, we have compared the trajectories of cells with their division timing (C). We found three phases: phase 1, before 17:20 hAPF no deformation is observed; phase 2, between 17:20 and 21:20 hAPF the medial domain undergoes a contraction-elongation movement, and most cells of the scutellum medial domain move laterally without undergoing cell division; phase 3, after 21:20 hAPF the tissue expands in all directions (A').*
During these three phases cell divisions are aligned along the tissue medial-lateral axis. The comparison of the cell division rate with the magnitude of tissue deformation reveals that: (i) cell division rate, maximal in phase 1, does not correlate with the magnitude of tissue deformation, minimal in phase 1; (ii) the strongest contraction-elongation deformation of the scutellum medial domain (phase 2) occurs between two waves of

cell divisions (phases 1 and 3); (iii) during each wave of cell divisions (phases 1 and 3), the orientation of cell division does not correlate with that of tissue deformation rate. Together, these results argue against a role of cell division orientation in the contraction-elongation deformation of the scutellum medial region.

(**A,A'**) Local deformation rate averaged over 5 wt hemi-scutellum movies at 25°C between 13:20 and 26:40 hAPF, represented as ellipses: a direction of elongation is represented in red and contraction in blue. (A) Local deformation rate averaged between 17:20 and 21:20 hAPF. The solid and dashed rectangular boxes outline the domains where the kymograph in A' and the cell division orientation in B are measured, respectively. (A') Kymograph of the deformation rate in the medial domain of the scutellum (solid box in A). Note that the data presented in panels A-A' are extensions of the data presented in Fig. 2B. (**B**) Division rate: graph of the ensemble average number of cell divisions per frame and symmetrized rose plots of their orientation during the three phases of development measured in the dashed box in A, obtained by segmenting and tracking each individual cell between 13:20 and 26:40 hAPF. The number of cell divisions per frame was time averaged over 24 frames and ensemble averaged over 4 wt hemi-scutellum movies at 25°C (total cumulated over 4 movies: $n = 1591$ divisions, with an error rate estimated $< 1\%$ by visual inspection of each frame). (**C**) 50 min cell trajectories during contraction-elongation movements. Following the segmentation of a single time-lapse movie of the scutellum between 11:00 and 27:40 hAPF, cell lineages, timing of each division and cell trajectories were determined. Cell trajectories are color coded according to the number of cell divisions that each cell has undergone: pink for cells having divided once; blue for cells having divided twice; green (a few cells are visible between the macrochaetae) for the third wave of division which begins just before 22 hAPF (Movie S2B). The rectangular box (reference window, same as in fig. S4A) outlines the domain where cell division orientations are measured in (B). Scale bars: 10 μm (A); 10^{-3} min^{-1} (blue bars in A and A'); 20 μm (C).

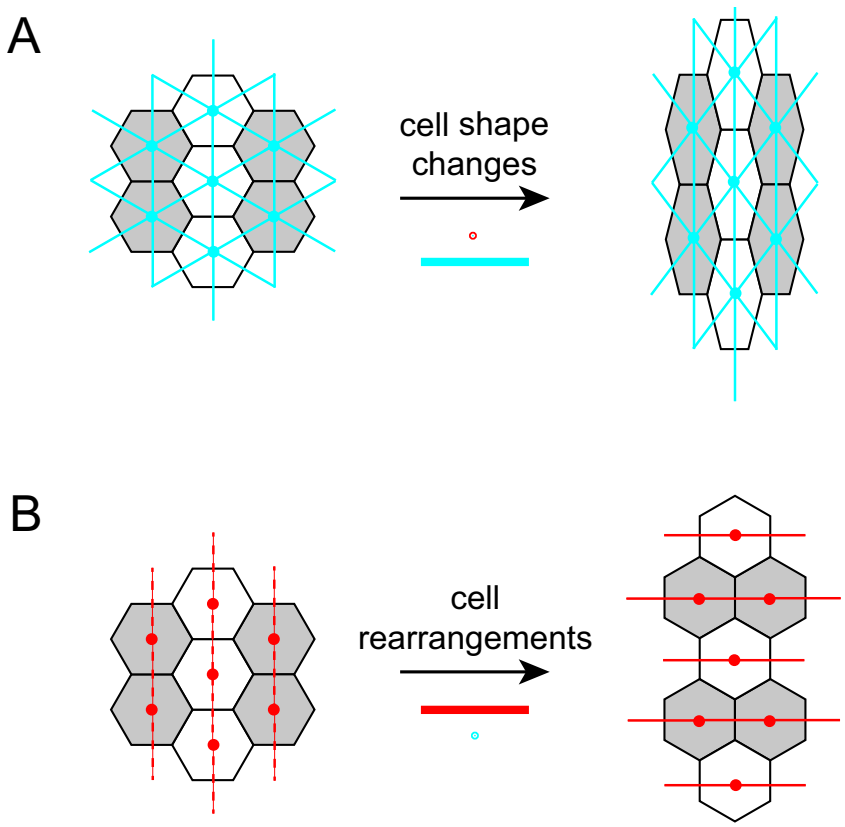

Figure S13. Representation of quantitative analysis of cell rearrangements and cell shape changes. *Between the initial (left) and final (right) images, a tissue domain is undergoing a contraction (here along the horizontal axis) accompanied by an elongation in the perpendicular direction. Such tissue domain shape change may arise from processes such as cell rearrangements or changes of individual cell shapes. For simplicity, cells are here sketched as identical, and both processes are depicted separately, but the same quantitative analysis was performed on our experimental movies of the developing Drosophila dorsal thorax where both processes may contribute together to local tissue deformations.*

(**A**) Cell shape changes, represented by a cyan bar quantifying the number, the magnitude and the direction of cell contraction (here horizontal). Since in this example all cells conserve their neighbors (thin cyan lines), cell rearrangements have no contribution (red dot). (**B**) Round of oriented cell rearrangements: horizontal junctions shrink and disappear (corresponding cell-center links are indicated by dashed red lines). New vertical junctions appear and elongate (corresponding cell-center links are indicated by thin cyan lines). Cell rearrangements are represented by a red bar quantifying the number, the length and direction of lost junctions / new links (here horizontal). Since in this example all cells end up with the same shape as in their initial state, cell shape changes have no contribution (cyan dot).

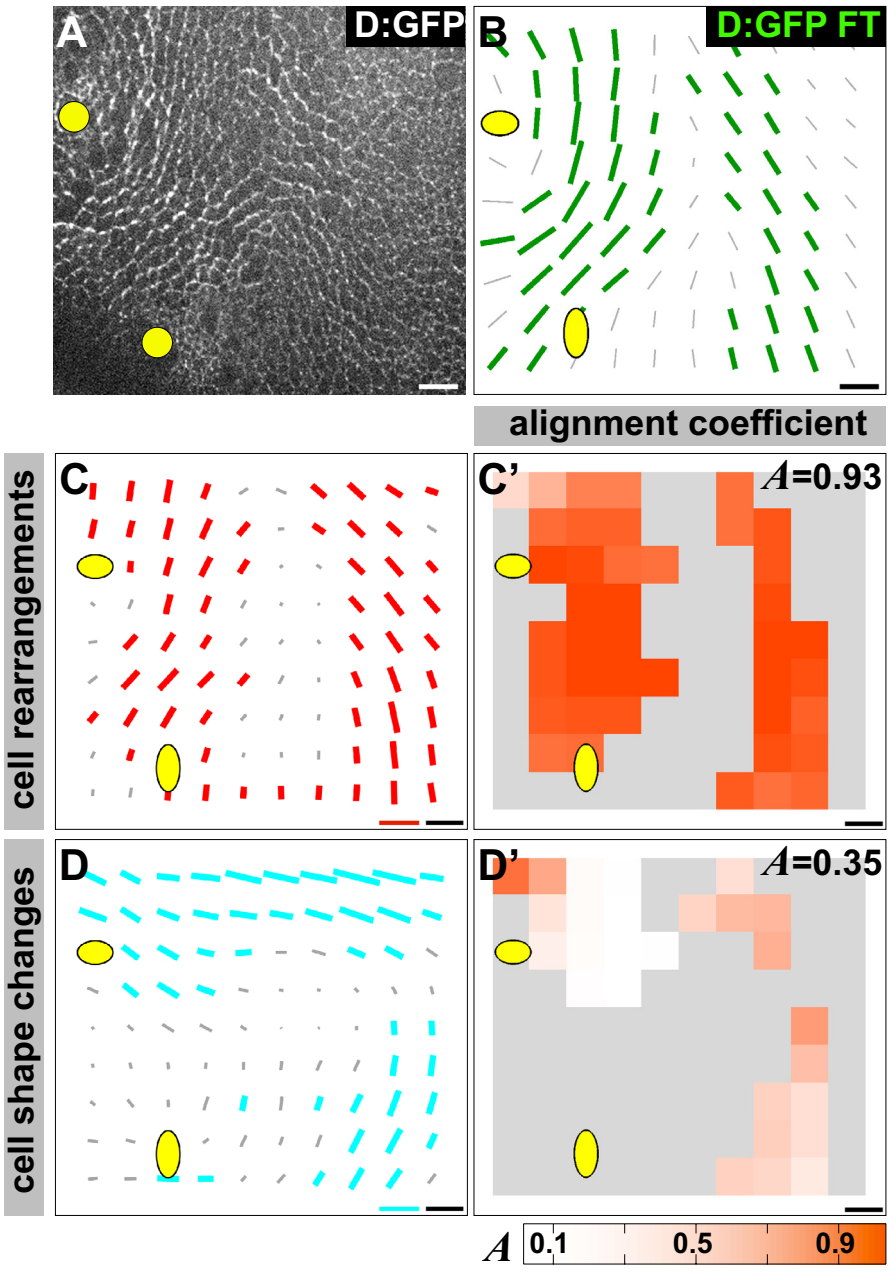

Figure S14. Dachs polarization, as quantified by Fourier Transform (FT), strongly correlates with cell rearrangements and poorly correlates with cell shape changes.

(**A,B**) D:GFP pattern: (A) snapshot, the same as Fig. 2A, Fig. 4A, fig. S5A and fig. S10I. (B) Averaged map of FT, the same as Fig. 4B and fig. S10J. (**C,C'**) Maps of cell rearrangements in wt (C) and of their alignment coefficients with the D:GFP FT (C'). (**D,D'**) Same for cell shape changes. Significant data: color bars; other: gray bars (C,D). The local score of the alignment with D:GFP FT (C',D') is coded in orange from 0 for fully anti-correlated, to 1 for fully correlated, through 0.5 for non correlated. The overall score A is indicated. Gray squares indicate IC-boxes where data were not significant: they were not included in the calculation of A. Scale bars: 10 μm (A-D'), 1 μm^2 min^{-1} (red bar in C, cyan bar in D).

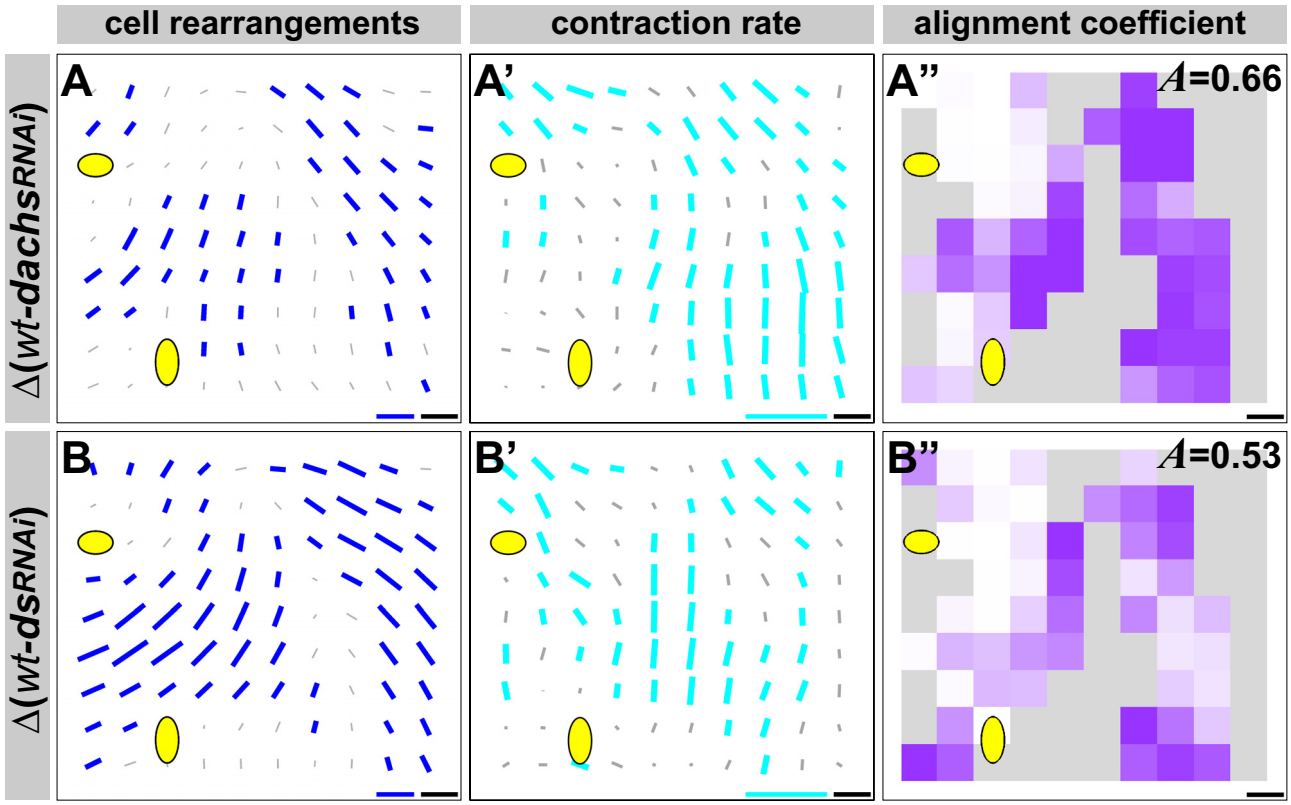

Figure S15. Maps of local cell shape changes and of their correlation with contraction rates in *dachs*^{RNAi} or *ds*^{RNAi} mutant conditions.

(**A-B**) Specific contribution of *dachs*^{RNAi} (A) and *ds*^{RNAi} (B) to contraction rate, calculated according to the right hand side of Eq. (11). Same panels as in Fig. 4C,D. (**A'-B'**) Specific contribution of *dachs*^{RNAi} (A') and *ds*^{RNAi} (B') to cell shape changes: the cell shape change (explained in section 4.2) of *dachs*^{RNAi} or *ds*^{RNAi} mutant condition is subtracted from that of wt one. (**A"-B"**) Maps of the alignment coefficient between the specific contraction rate (A-B) and cell shape changes (A'-B') in *dachs*^{RNAi} (A") and *ds*^{RNAi} (B"). Data are represented only where D:GFP has a significantly non-zero FT signal. The local score of the mutual alignment is coded in purple from 0 for fully anti-correlated, to 1 for fully correlated, through 0.5 for non correlated. The overall score A is indicated: cell shape changes score 0.66 and 0.53, while cell rearrangements score a significantly higher ($p < 10^{-16}$) correlation at 0.8 and 0.77, respectively (Fig. 4E',F'). Gray squares indicate IC-boxes where FT data were not significant: they were not included in the calculation of A. Scale bars: 10 μm, 5.5×10^{-4} min^{-1} (blue bars in A, B), 1 μm^2 min^{-1} (cyan bars in A', B').

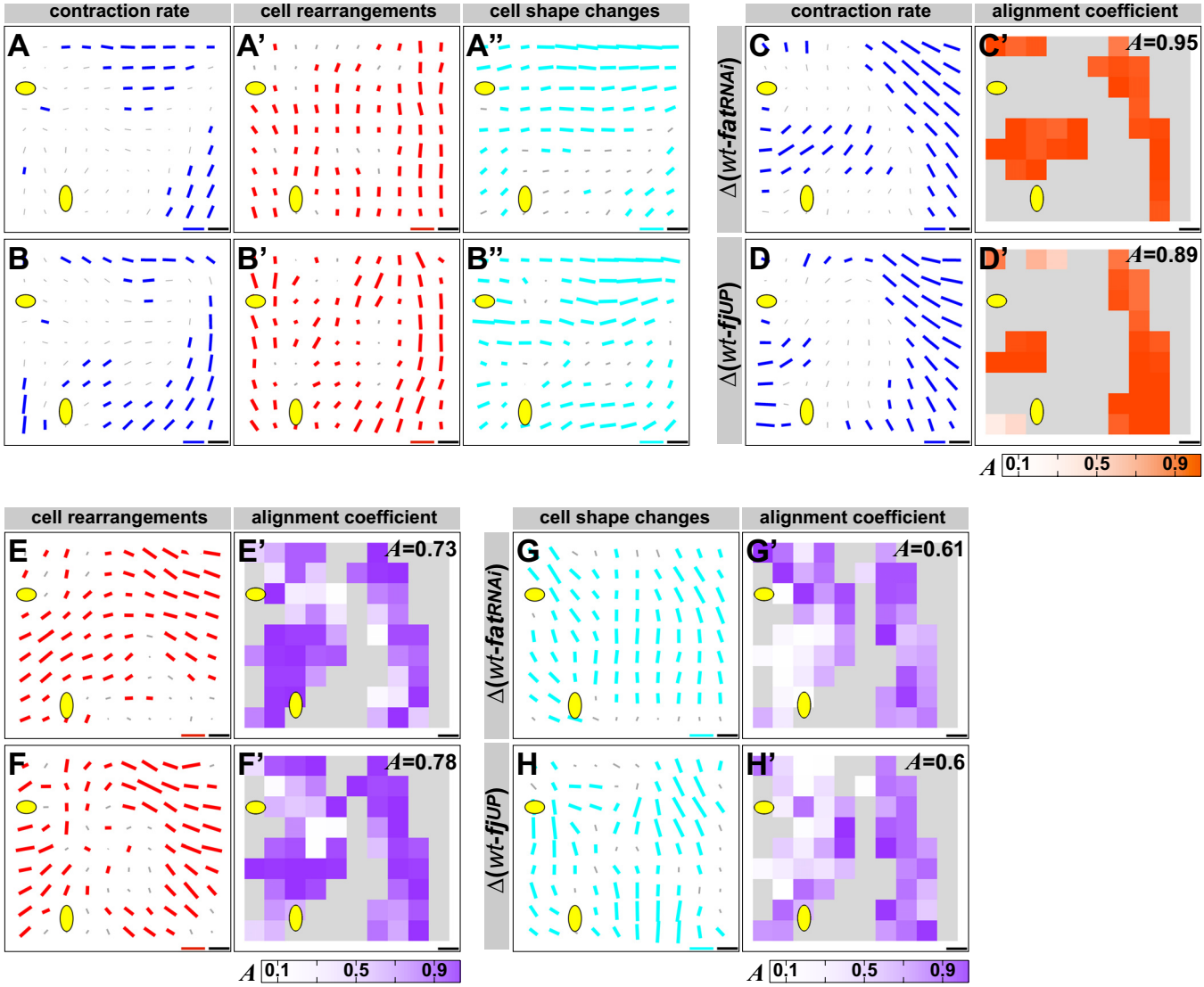

Figure S16. Analysis of tissue contractions, cell rearrangements and cell shape changes in fj^{UP} and fat^{RNAi} scutella. *To facilitate the comparison with Dachs and Ds analyses, the legend is the same as in the corresponding figures: (A-B") fig. S11B-C", (C-F') Fig. 4C-F', (G-H') fig. S15A"-B". Note the similarity of Fat data with Dachs and Ds. This analysis of cell rearrangements and cell shape changes in fj^{UP} and fat^{RNAi} scutella confirmed the results obtained for $dachs^{RNAi}$ and ds^{RNAi}, namely that Dachs controls tissue contraction mainly by promoting cell rearrangements along its polarization pattern. Cell rearrangements score at 0.73 and 0.78 (E',F'), indicating significantly higher ($p < 10^{-12}$) correlations than cell shape changes which score at 0.61 and 0.6, respectively (G',H').*

(**A-H'**) Maps for $fj^{UP}$and fat^{RNAi}. Color-coded maps represent alignment coefficients between the difference in contraction rate and: the D:GFP FT (C',D': orange); cell rearrangements within the D:GFP FT pattern (E',F': purple); and cell shape changes within the D:GFP FT pattern (G',H': purple). Overexpression of *fj* partially abrogated D:GFP polarity mostly in the anterior part of the Λ-shaped domain and, accordingly, significant differences in the convergence rate were observed mostly in the anterior part (D).

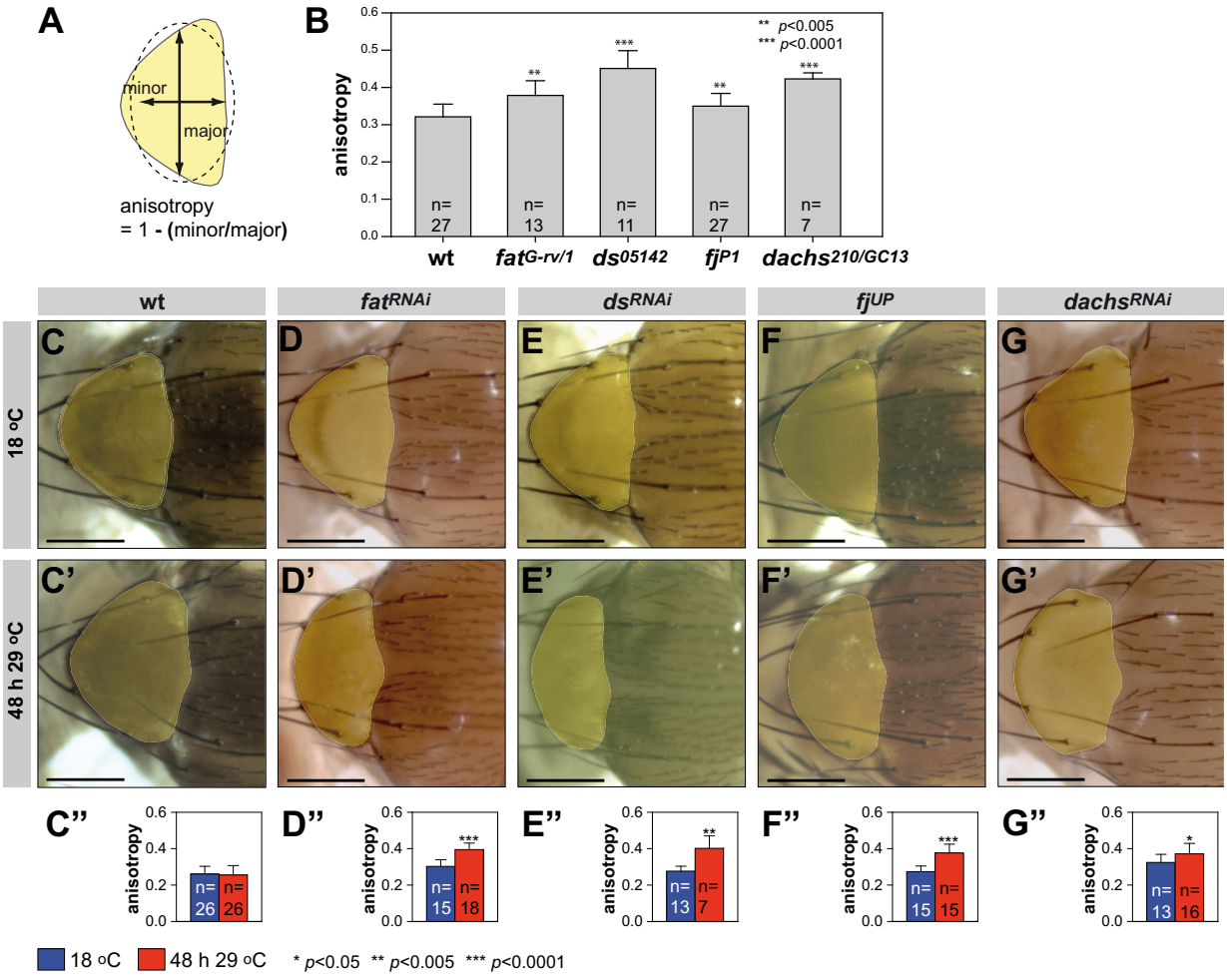

Figure S17. The Fat/Ds/Fj/Dachs pathway modifies the scutellum shape. *fat^{RNAi} (D-D"), ds^{RNAi} (E-E"), fj^{UP} (F-F"), and $dachs^{RNAi}$ (G-G") mutants in which we temporally abrogated the gradient of fj expression or abrogated the function of ds, fat or dachs using the GAL80ts (13) resulted in the elongation of the adult scutellum along its medial-lateral axis and in a higher anisotropy (defined in A). fat, ds, fj and dachs hypomorphic alleles also affect tissue anisotropy (B). Since these genes have a well-characterized role in growth/proliferation of third instar imaginal discs, conditional expression of $dachs^{RNAi}$ hairpins or overexpression constructs at the end of the larval life are in our view a better demonstration of the role of the Fat/Ds/Fj pathway during pupal development. These medial-lateral elongations agree with the respective differences in contraction rates: the medio-lateral contraction in wt is replaced in mutants with an antero-posterior contraction (Fig. 4 and fig. S11).*

(**A-B**) Definition (A) and measurement (B) of scutellum anisotropy for hypomorphic mutations of *fat*, *ds*, *fj* and *dachs*. (**C-G"**) Adult scutella (shaded yellow domains in C-G') and measurements (C"-G") of their anisotropy for wt (C-C"), fat^{RNAi} (D-D"), ds^{RNAi} (E-E"), fj^{UP} (F-F"), and $dachs^{RNAi}$ (G-G") adults that were raised at 18°C, used as controls (C-G), or that were transferred to 29°C for a period of 48 h (C'-G'). Change in temperature from 18°C to 29°C did not affect the wt scutellum shape. p values were determined by Student's t-test. Scale bars: 250 μm.

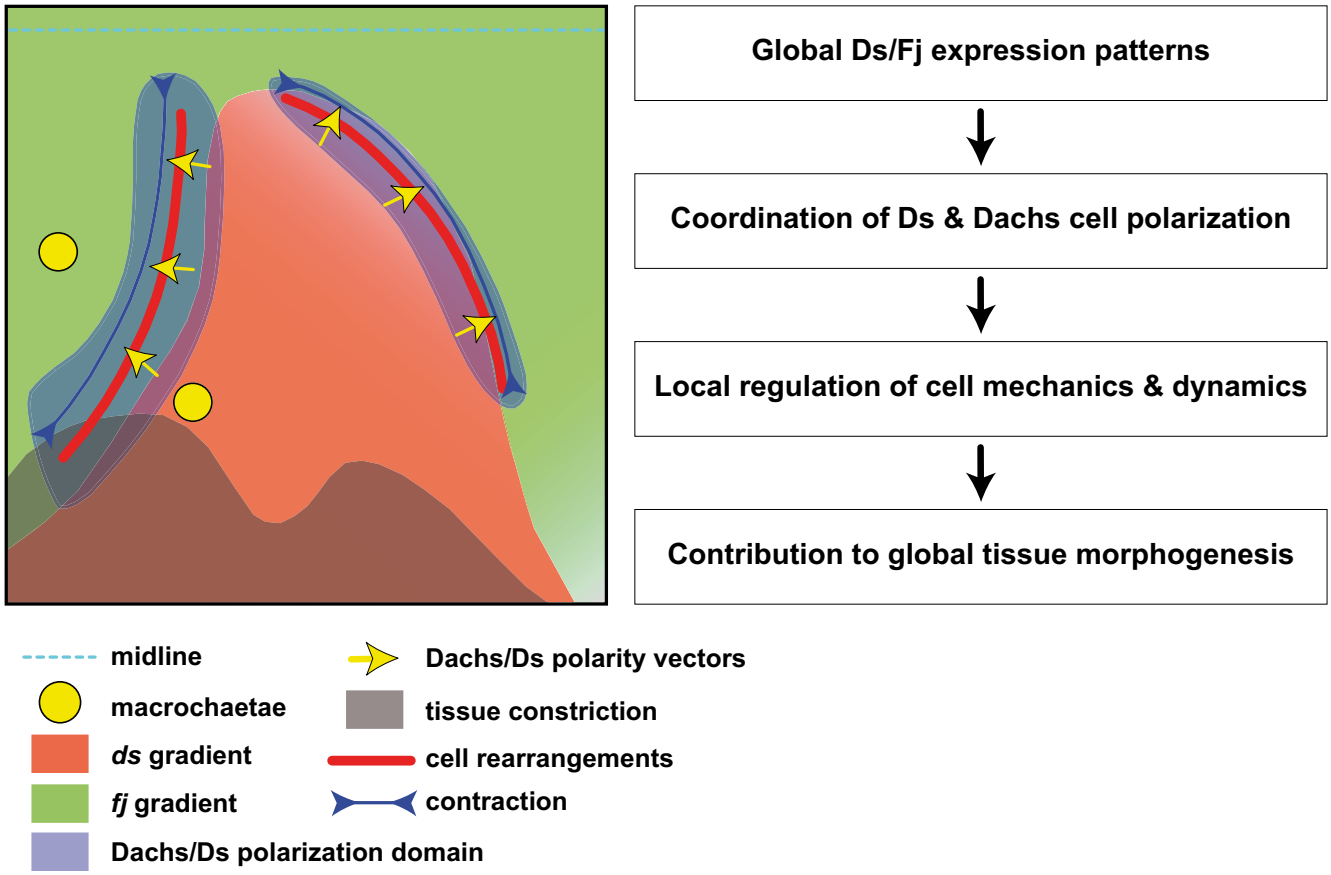

Figure S18. Graphical summary. *Scheme of a Drosophila hemi-scutellum during metamorphosis (anterior to the right). Positional landmarks are indicated: macrochaetae as yellow dots, and midline as a magenta dashed line. The tissue domain that undergoes strong constriction is marked in gray. In the scutellum, tissue-wide expression gradients of Ds (red) and Fj (green) exists. These opposing gradients define regions in which Ds is planar polarized (blue) and the orientation of the polarization (towards high Fj, yellow arrows). In turn Ds polarization results in the polarization of the Dachs myosin. Their local polarization produces an anisotropic distribution of cell junction tensions, which contribute to increasing the contraction rates (blue lines) along the lines of Ds and Dachs planar polarization to shape the epithelial tissue mainly by oriented cell rearrangements (red lines).*

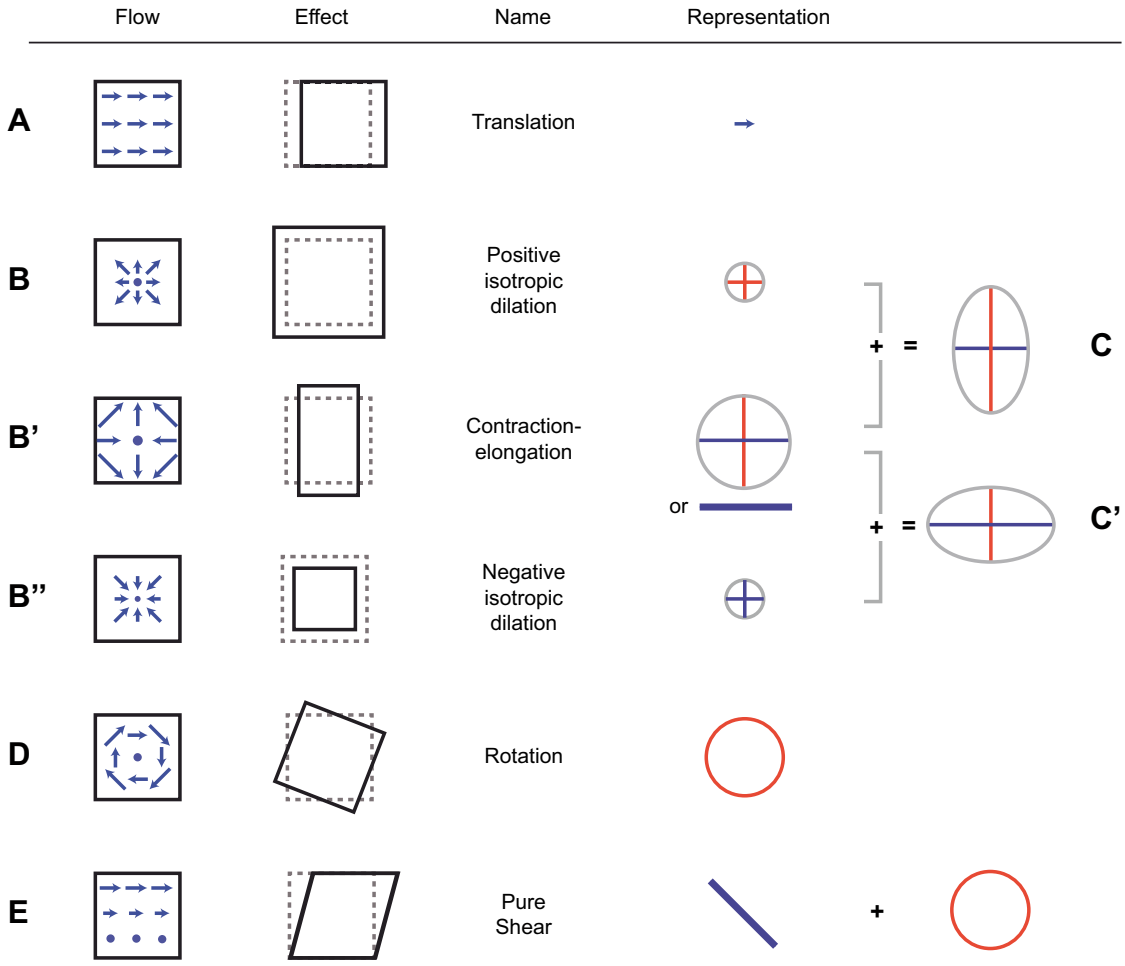

Figure S19. Local deformation rate, contraction-elongation rate, and rotation rate. *The velocity gradient is decomposed into its symmetric and its anti-symmetric parts (31, 32). The deformation rate, related to the symmetric part of the velocity gradient, reflects changes in tissue size and shape. From it we separate the size changes to extract the contraction-elongation rate, which directly reflects effective changes in tissue shape. The local rotation rate or vorticity, related to the anti-symmetric part of the velocity gradient, does not by itself contribute to tissue shape change. Accordingly, contraction-elongation and rotation are two quantities that can vary independently. If the velocity gradient has no symmetric part, the tissue rotates as a whole, and there is no tissue shape change. If the rotation rate is spatially heterogeneous, the velocity gradient has non-zero symmetric and anti-symmetric parts: in that case there are simultaneously a shape change and a rotation, but they are not related, and again the rotation is not directly involved in tissue shape change. We thus purposedly exclude the rotation from our analysis of morphogenetic changes, and use it only to synchronise the movies (section 2.2.2 and fig. S4). To avoid ambiguities we do not use the words "shear rate" which in the literature indicate either a symmetrized (B') or a non-symmetrized (E) velocity gradient.*

Schematic, not drawn to scale, of the notations and definitions used in the text. (**A**) A global translation of a tissue domain does not contribute to its shape or size change. (**B-B"**) A positive isotropic dilation (B) has two equal positive eigenvalues (in red). A "contraction-elongation" (B') represents perpendicular contraction

and elongation with the same amplitude: it has two opposite eigenvalues (red for positive, blue for negative), and can be represented indifferently by a red bar and a blue one within a circle, or only by the blue bar for clarity. A negative isotropic dilation (B") has two equal negative eigenvalues (in blue). Dilations contribute to tissue size change, contraction-elongation to tissue shape change. (**C-C'**) Combining a dilation and a contraction-elongation results in a deformation rate with a larger positive eigenvalue (C=B+B') or a larger negative eigenvalue (C'=B'+B"). Since B', C and C' correspond to the same contraction-elongation, they are represented by the same blue bar. (**D**) A rotation is represented by a circle, here red for clockwise (else, blue for counter-clockwise). It does not by itself contribute to tissue shape or size change. (**E**) "Pure shear" or "simple shear" can be decomposed in a contraction-elongation, which changes the shape, and rotation, which changes the orientation (E=B'+D). The contraction-elongation is represented by a blue bar in the direction of contraction. For details see section 2.1.2.

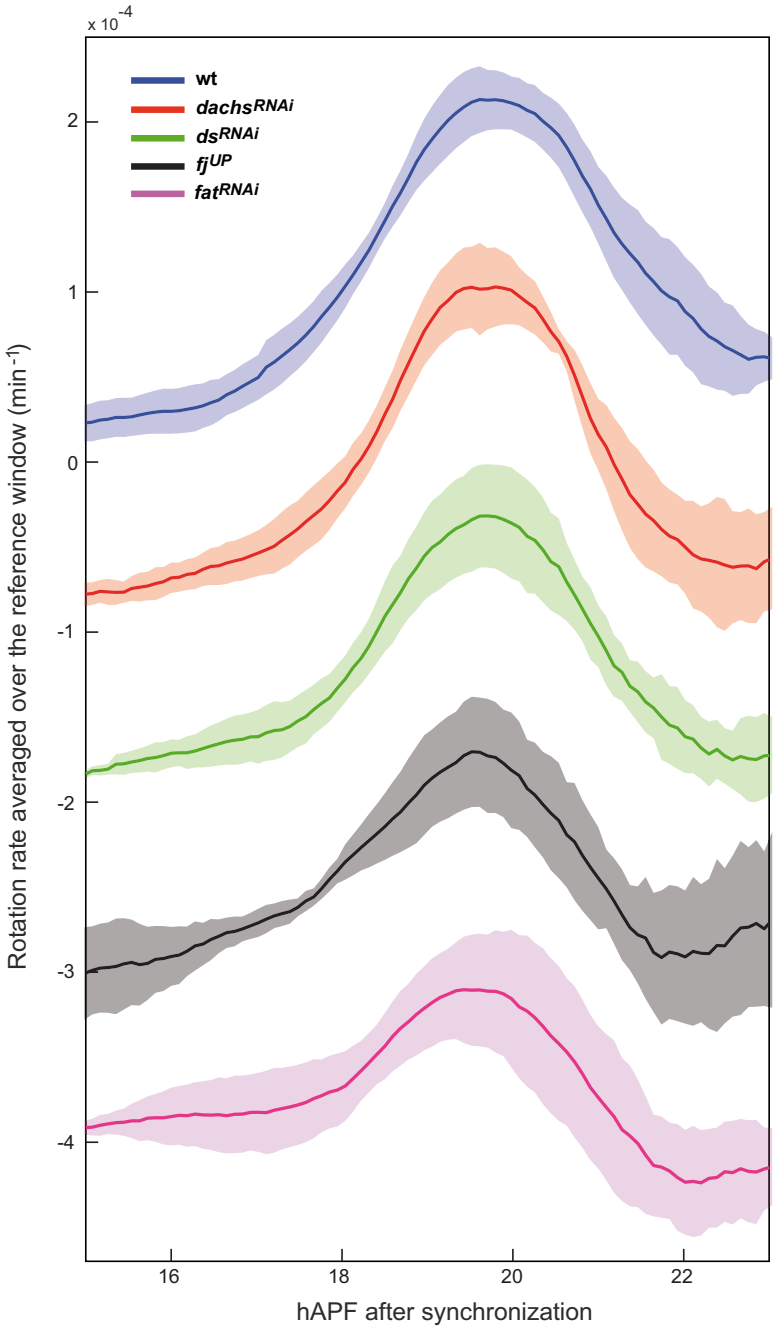

Figure S20. Rotation rate in wt and mutant scutella during morphogenesis. *Qualitatively the peak of rotation rate in mutant scutella is the same as in wt, but quantitatively its amplitude is reduced.*

Mean value (thick line) ± ensemble standard deviation (shade) versus hAPF after synchronization. The rotation rate was space averaged over the reference window (fig. S4) and ensemble averaged over n movies of the same genotype. Blue, wt, $n = 11$ (same data as fig. S4B"); red, $dachs^{RNAi}$, $n = 5$; green, ds^{RNAi}, $n = 6$; black, fj^{UP}, $n = 4$; magenta, fat^{RNAi}, $n = 5$. Curves are vertically shifted by 10^{-4} min^{-1} for clarity.

5.2 Supporting movie captions

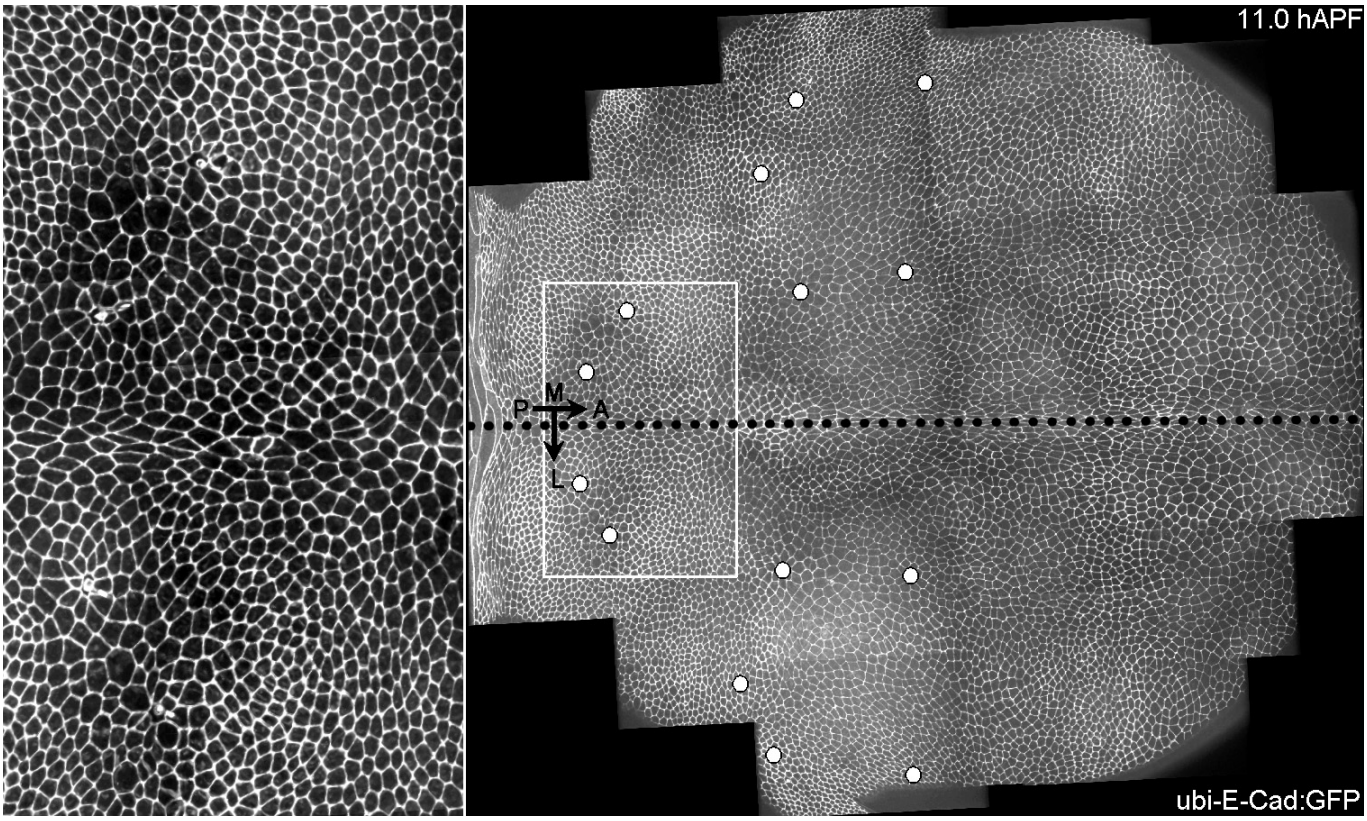

Movie S1. *Drosophila* pupa dorsal thorax tissue expressing E-Cad:GFP to label apical cell junctions, imaged by multi-position confocal microscopy (24 positions at a 5 min time resolution) between 11 and 35 hAPF. The boxed region, highlighting the scutellum, is magnified at the left. The positions of the macrochaetae and of the midline are indicated by white circles and by a black dotted line, respectively. Arrows indicate the A/P and M/L axes. For compression reasons, these images have half the resolution of original movie.

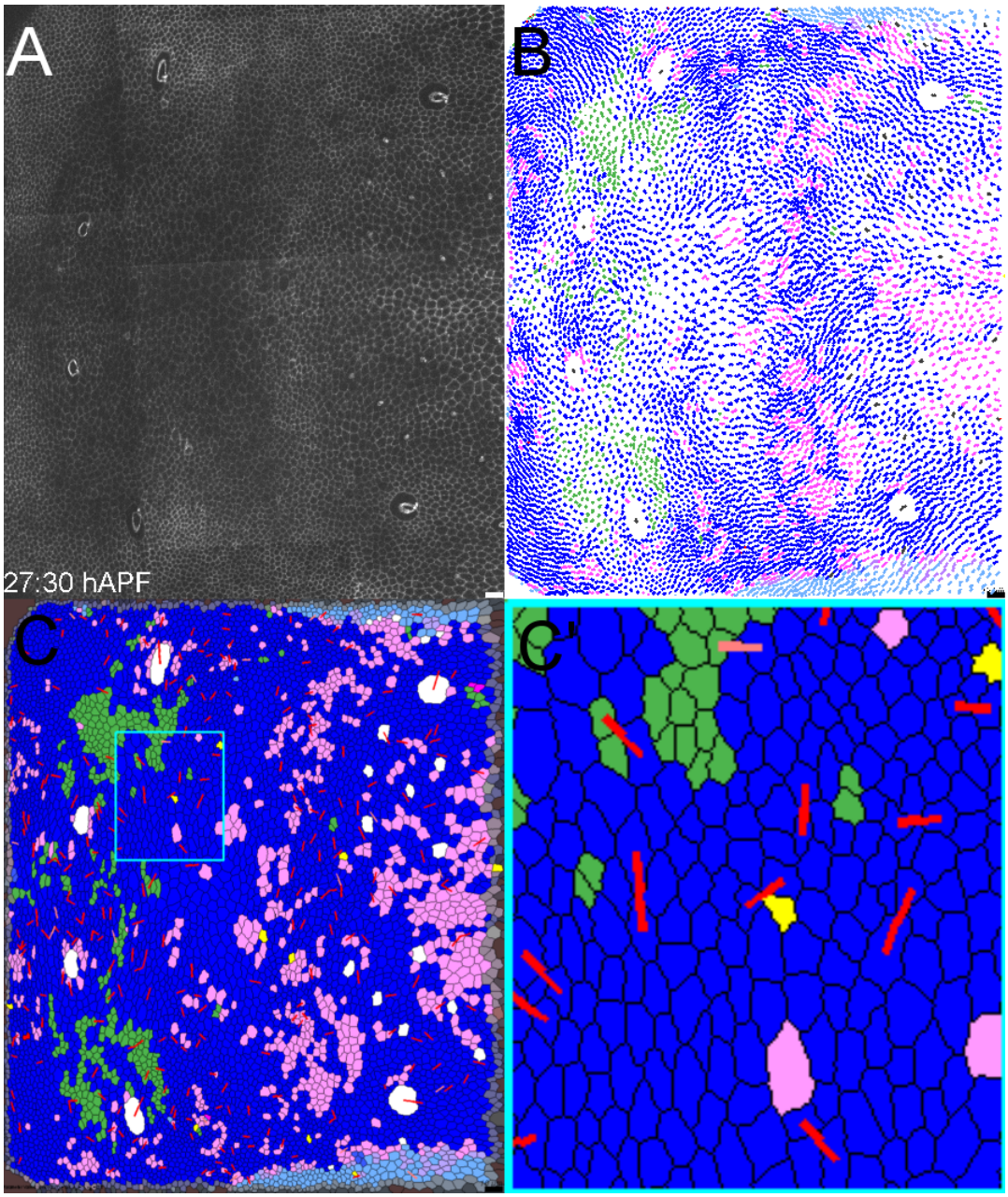

Movie S2. Tracking of cell dynamics in the scutellum and the posterior scutum. Note that, in order to show the full color code, the above still image is the last image of the movie. **(A)** Dorsal thorax tissue labeled with E-Cad:GFP and imaged by multi-position confocal microscopy at a 5 min time resolution between 11:30 and 27:30 hAPF. **(B)** Tracking of cell trajectories. **(C)** Tracking of cell divisions, apoptoses and rearrangements. Each cell is color coded according to the number of cell divisions that it undergoes during the movie: pink for cells having divided once; blue for cells having divided twice; green for the third wave of division. Links used to calculate cell rearrangement matrix (section 4.2) are shown as lines. Two cells which are in contact in an image, and not in the next one, correspond to a lost link, plotted as a yellow line. Two cells which get in contact in an image, and were not in contact in the previous one, correspond to a gained link, plotted as a red line. Links involving a four-fold vertex are shown in lighter colours. Yellows zones indicate an apoptosis or delamination (which we do not distinguish). Light blue cells indicate new cells that entered the field of view. **(C')** Blow up of the region delimited in C by a cyan square. Scale bars (A-C): 10 μm.

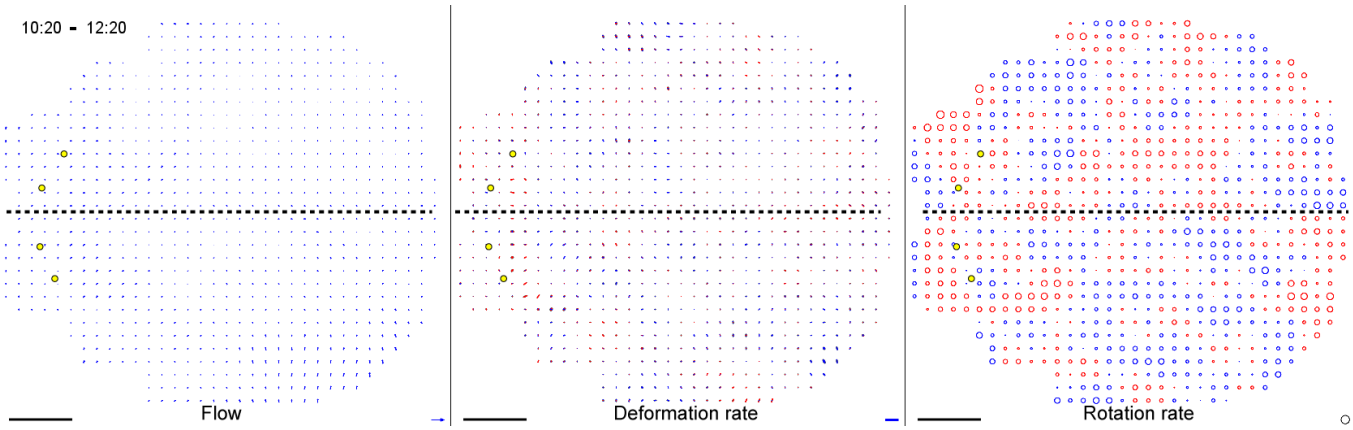

Movie S3. Local tissue flow, deformation rate and rotation rate measured on Movie S1. Left: flow velocity is represented as arrows. Middle: deformation rate is represented as ellipses; a direction of elongation is represented in red and contraction in blue. Right: rotation rate is represented by circle diameters; clockwise is represented in red and counter-clockwise in blue. For compression reasons, only one image every half hour is shown. Scale bars: 100 μm (black bars), 9×10^{-2} μm min^{-1} (arrow, left), 2.4×10^{-3} min^{-1} (blue bar, middle), 8×10^{-5} min^{-1} (circle, right).

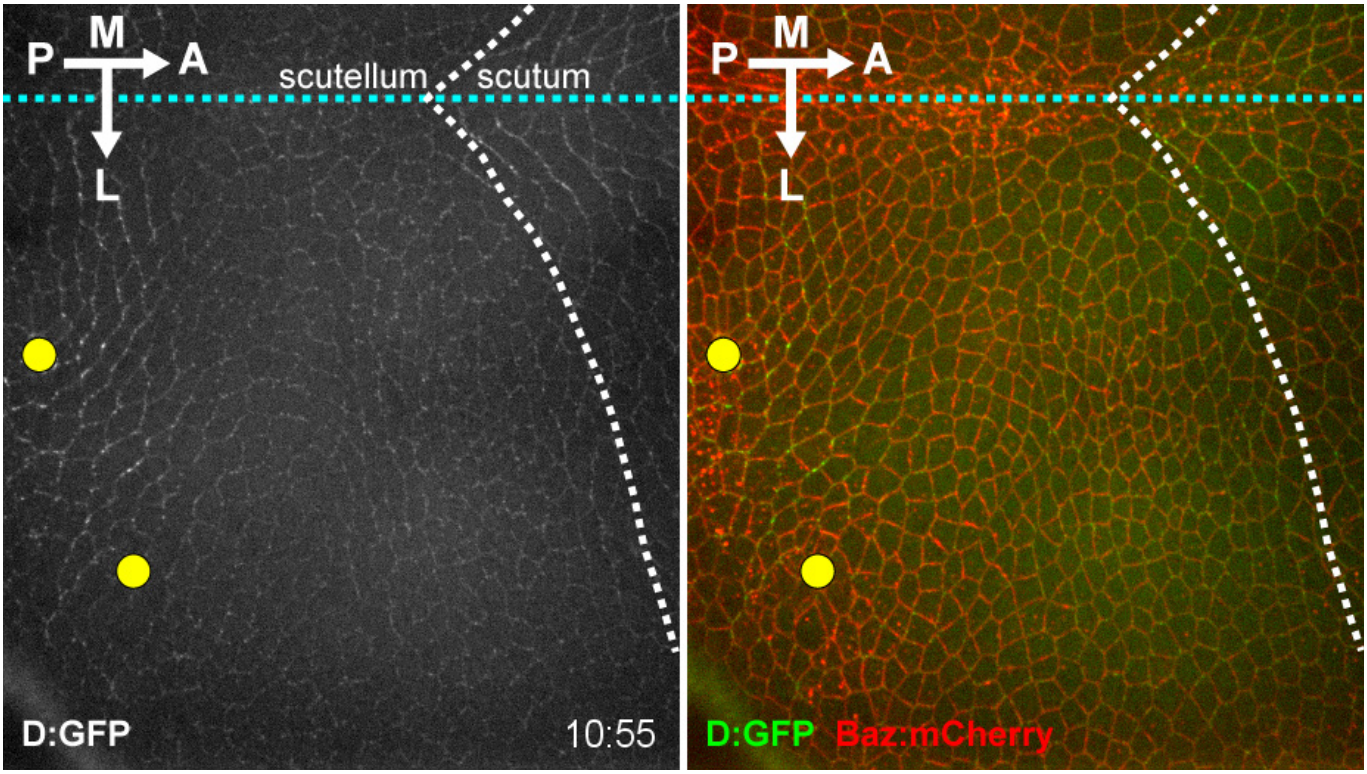

Movie S4. Scutellum labeled with D:GFP and Baz:mCherry during morphogenesis (11 to 26 hAPF). The positions of the macrochaetae and of the midline are indicated by yellow circles and by a cyan dashed line, respectively. Arrows indicate the A/P and M/L axes.

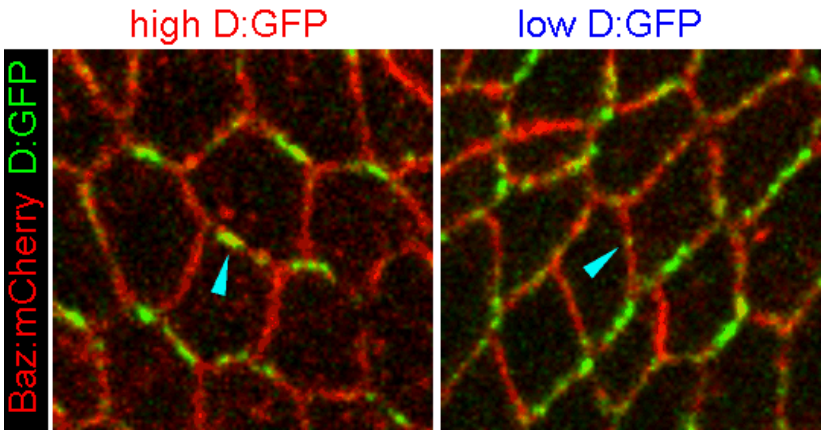

Movie S5. Representative movies of cell junction ablations with high (left) or low (right) D:GFP signal in the scutellum of pupae expressing D:GFP and Baz:mCherry.

References

[1] H. Matakatsu, S. S. Blair, Interactions between Fat and Dachsous and the regulation of planar cell polarity in the *Drosophila* wing. *Development* **131**, 3785-3794 (2004).

[2] M. P. Zeidler, N. Perrimon, D. I. Strutt, The four-jointed gene is required in the *Drosophila* eye for ommatidial polarity specification. *Curr. Biol.* **9**, 1363-1372 (1999).

[3] H. Oda, S. Tsukita, Real-time imaging of cell-cell adherens junctions reveals that *Drosophila* mesoderm invagination begins with two phases of apical constriction of cells. *J. Cell Sci.* **114**, 493-501 (2001).

[4] J. Huang, W. Zhou, W. Dong, A. M. Watson, Y. Hong, Directed, efficient, and versatile modifications of the *Drosophila* genome by genomic engineering. *Proc. Natl. Acad. Sci. U. S. A* **106**, 8284-8289 (2009).

[5] M. H. Brodsky, H. Steller, Positional information along the dorsal-ventral axis of the *Drosophila* eye: graded expression of the four-jointed gene. *Dev. Biol.* **173**, 428-446 (1996).

[6] Y. Mao *et al.*, Dachs: an unconventional myosin that functions downstream of Fat to regulate growth, affinity and gene expression in *Drosophila*. *Development* **133**, 2539-2551 (2006).

[7] E. Cho *et al.*, Delineation of a Fat tumor suppressor pathway. *Nat. Genet.* **38**, 1142-1150 (2006).

[8] A. Martin, M. Kaschube, E. Wieschaus, Pulsed contractions of an actin-myosin network drive apical constriction, *Nature* **457**, 495-499 (2009).

[9] K. G. Golic, S. Lindquist, The FLP recombinase of yeast catalyzes site-specific recombination in the *Drosophila* genome. *Cell* **59**, 499-509 (1989).

[10] T. Xu, G. M. Rubin, Analysis of genetic mosaics in developing and adult *Drosophila* tissues. *Development* **117**, 1223-1237 (1993).

[11] K. Basler, G. Struhl, Compartment boundaries and the control of *Drosophila* limb pattern by hedgehog protein. *Nature* **368**, 208-214 (1994).

[12] A. H. Brand, N. Perrimon, Targeted gene expression as a mean of altering cell fates and generating dominant phenotypes. *Development* **118**, 401-415 (1993).

[13] S. E. McGuire, P. T. Le, A. J. Osborn, K. Matsumoto, R. L. Davis, Spatiotemporal rescue of memory dysfunction in *Drosophila*. *Science* **302**, 1765-1768 (2003).

[14] K. J. Venken, Y. He, R. A. Hoskins, H. J. Bellen, P[acman]: a BAC transgenic platform for targeted insertion of large DNA fragments in *Drosophila* melanogaster. *Science* **314**, 1747-1751 (2006).

[15] K. J. Venken *et al.*, Versatile P[acman] BAC libraries for transgenesis studies in *Drosophila* melanogaster. *Nat. Methods* **6**, 431-434 (2009).

[16] R. Benton, D. St Johnston, *Drosophila* PAR-1 and 14-3-3 inhibit Bazooka/PAR-3 to establish complementary cortical domains in polarized cells. *Cell* **115**, 691-704 (2003). Erratum in *Cell* **116**, 139 (2004).

[17] J. Langevin *et al.*, Lethal giant larvae controls the localisation of the Notch signalling regulators Numb, Neuralized and Sanpodo in *Drosophila* sensory organ precursor cells, *Curr. Biol.* **15**, 955-962 (2005).

[18] M. Segalen *et al.*, The Fz-Dsh planar cell polarity pathway induces oriented cell division via Mud/NuMA in *Drosophila* and *Zebrafish*. *Dev. Cell* **19**, 740-752 (2010).

[19] H. Strutt, J. Mundy, K. Hofstra, D. Strutt, Cleavage and secretion are not required for Four-jointed function in *Drosophila* patterning. *Development* **131**, 881-890 (2004).

[20] C. H. Yang, J. D. Axelrod, M. A. Simon, Regulation of Frizzled by fat-like cadherins during planar polarity signaling in the *Drosophila* compound eye. *Cell* **108**, 675-688 (2002).

[21] D. Ma, C. H. Yang, H. McNeill, M. A. Simon, J. D. Axelrod, Fidelity in planar cell polarity signalling. *Nature* **421**, 543-547 (2003).

[22] H. F. Clark *et al.*, Dachsous encodes a member of the cadherin superfamily that controls imaginal disc morphogenesis in *Drosophila*. *Genes Dev.* **9**, 1530-1542 (1995).

[23] N. David *et al.*, *Drosophila* Ric-8 regulates Gαi cortical localization to promote Gαi-dependent planar orientation of the mitotic spindle during asymmetric cell division. *Nat. Cell Biol.* **7**, 1083-1090 (2005).

[24] M. S. Hutson *et al.*, Plasma and cavitation dynamics during pulsed laser microsurgery *in vivo*. *Phys. Rev. Lett.* **99**, 158104-158108 (2007).

[25] R. Farhadifar, J.-C. Röper, B. Aigouy, S. Eaton, F. Jülicher, The influence of cell mechanics, cell-cell interactions, and proliferation on epithelial packing. *Curr. Biol.* **17**, 2095-2104 (2007).

[26] M. Rauzi, P. Verant, T. Lecuit, P.-F. Lenne, Nature and anisotropy of cortical forces orienting *Drosophila* tissue morphogenesis. *Nat. Cell Biol.* **10**, 1401-1410 (2008).

[27] M. S. Hutson *et al.*, Combining laser microsurgery and finite element modeling to assess cell-level epithelial mechanics. *Biophys. J.* **97**, 3075-3085 (2009).

[28] M. Rauzi, P.-F. Lenne, Cortical forces in cell shape changes and tissue morphogenesis. *Curr. Top. Dev. Biol.* **95**, 93-144 (2011).

[29] J. Boulanger *et al.*, Patch-based nonlocal functional for denoising fluorescence microscopy image sequences. *IEEE Trans. Med. Imaging* **29**, 442-454 (2010).

[30] G. Blanchard *et al.*, Tissue tectonics: morphogenetic strain rates, cell shape change and intercalation. *Nat. Methods* **6**, 458-464 (2009).

[31] Y.C. Fung, *Biomechanics: mechanical properties of living tissues* (Springer-Verlag, New York, 1993).

[32] G. K. Batchelor, *An introduction to fluid dynamics* (Cambridge Univ. Press, Cambridge, 2000).

[33] M. Raffel, C.E. Willert, S.T. Wereley, J. Kompenhans, *Particle Image Velocimetry: A Practical Guide* (Springer-Verlag, New York, 2007).

[34] M. Gho, Y. Bellaïche, F. Schweisguth, Revisiting the *Drosophila* microchaete lineage: a novel intrinsically asymmetric cell division generates a glial cell. *Development* **126**, 3573-3584 (1999).

[35] R. C. Gonzalez, R. E. Woods, S. L. Eddins, *Digital Image processing using MATLAB* (Gatesmark, ed. 2, 2009).

[36] T. Lecuit, P.-F. Lenne, Cell surface mechanics and the control of cell shape, tissue patterns and morphogenesis. *Nature Rev. Mol. Cell Biol.* **8**, 633-644 (2007).

[37] P. Marmottant *et al.*, The role of fluctuations and stress on the effective viscosity of cell aggregates *Proc. Natl. Acad. Sci. USA*, **106**, 17271-17275 (2009).

[38] D. Ambrosi, L. Preziosi, Cell adhesion mechanisms and stress relaxation in the mechanics of tumours. *Biomech. Model Mechanobiol.* **8**, 397-413 (2009).

[39] G. Forgacs, R. A. Foty, Y. Shafrir, M. S. Steinberg, Viscoelastic properties of living embryonic tissues: a quantitative study. *Biophys. J.* **74**, 2227-2234 (1998).

[40] R. Foty, G. Forgacs, C. Pfleger, M. Steinberg, Liquid properties of embryonic tissues: measurement of interfacial tensions. *Phys. Rev. Lett.* **72** 2298-2301 (1994).

[41] K. Guevorkian, D. Gonzalez-Rodriguez, C. Carlier, S. Dufour, F. Brochard-Wyart, Mechanosensitive shivering of model tissues under controlled aspiration. *Proc. Natl. Acad. Sci. USA.* **108**, 13387-13392 (2011).

[42] J. Ranft *et al.*, Fluidization of tissues by cell division and apoptosis. *Proc. Natl. Acad. Sci. USA.* **107**, 20863-20868 (2010).

[43] L.D. Landau, E.M. Lifshitz, *Fluid Mechanics* (2nd ed.), Butterworth-Heinemann (Oxford, 1987).

[44] D. A. Reinelt, A. M. Kraynik, Simple shearing flow of dry soap foams with tetrahedrally close-packed structure, *J. Rheol.* **44**, 453-471 (2000).

[45] J. Neyman, Outline of a Theory of Statistical Estimation Based on the Classical Theory of Probability, *Philos. Trans. Roy. Soc. London A* **236**, 333–380 (1937).

[46] F. Graner, B. Dollet, C. Raufaste, P. Marmottant, Discrete rearranging disordered patterns, part I: robust statistical tools in two or three dimensions. *Eur. Phys. J. E* **25**, 349-369 (2008).

[47] B. Aigouy *et al.* Cell flow reorients the axis of planar polarity in the wing epithelium of *Drosophila*. *Cell* **142**, 773-786 (2010).

[48] M. Aubouy, Y. Jiang, J. A. Glazier, F. Graner, A texture tensor to quantify deformations. *Granular Matt.* **5**, 67-70 (2003).

[49] L. Butler *et al.*, Cell shape changes indicate a role for extrinsic tensile forces in *Drosophila* germ-band extension. *Nat. Cell Biol.* **11**, 859-864 (2009).

[50] D. Rogulja, C. Rauskolb, K. D. Irvine, Morphogen control of wing growth through the Fat signaling pathway. *Dev. Cell* **15**, 309-321 (2008).

[51] H. Matakatsu, S. S. Blair, The DHHC palmitoyltransferase approximated regulates Fat signaling and Dachs localization and activity. *Curr. Biol.* **18**, 1390-1395 (2008).

[52] H. Strutt, D. Strutt, Nonautonomous planar polarity patterning in *Drosophila*: dishevelled-independent functions of frizzled. *Dev. Cell* **3**, 851-863 (2002).

[53] J.H. Zar, Biostatistical Analysis, 4th edition, Prentice Hill (1999).

[54] P. Berens, CircStat: A MATLAB Toolbox for Circular Statistics. *J. Stat. Soft.* **31**, 1-21 (2009).

[55] G. Tzolovsky, H. Millo, S. Pathirana, T. Wood, M. Bownes, Identification and phylogenetic analysis of *Drosophila melanogaster* myosins. *Mol. Biol. Evol.* **19**, 1041-1052 (2002).

[56] A. Mehta *et al.*, Myosin-V is a processive actin-based motor, *Nature* **400**, 590-593 (1999).

[57] C. Veigel *et al.*, The motor protein myosin-I produces its working stroke in two steps, *Nature* **398** 530-532 (1999).

[58] P.-D. Coureux *et al.*, A structural state of the myosin V motor without bound nucleotide, *Nature* **425**, 419-423 (2003).

[59] E. De La Cruz, A. Wells, S. Rosenfeld, E. Ostap, L. Sweeney, The kinetic mechanism of myosin V, *Proc. Natl. Acad. Sci. USA.* **96**, 13726-13731 (1999).